DESIGNING HIGH PERFORMANCE STEAM TURBINES WITH ROTORDYNAMICS AS A PRIME CONSIDERATION

by

Stephen L. Edney

Manager, Core Technology

and

George M. Lucas

Vice President, Project Management

Dresser-Rand Company

Wellsville, New York

Stephen L. (Steve) Edney is Manager of Core Technology at Dresser-Rand's Wellsville Operation in New York. The Core Technology Department is responsible for the development, application, and trouble-shooting activities in aero/thermodynamics, materials science, rotordynamics, and stress analysis of steam turbines. Dr. Edney started his career in 1983 at GEC-Alsthom in the United Kingdom. He joined Dresser-Rand in 1991, and has since held supervisory positions in rotordynamics, and stress and vibration.

Dr. Edney received B.Sc. (1983) and Ph.D. (1990) degrees (Mechanical Engineering) from the University of Nottingham, England, and is a member of ASME and the Vibration Institute, and an associate member of IMechE. He holds one U.S. Patent, and has authored numerous technical papers in rotor and bearing dynamics.

George M. Lucas is Vice President of Project Management at Dresser-Rand's Wellsville Operation in New York. The Project Management Department is responsible for the overall project management on all steam turbine new unit orders, including application and project engineering, procurement, and scheduling. Mr. Lucas began his career as a Design Engineer with FMC Coffin Turbo Pump Operation. He subsequently joined Dresser-Rand's Steam Turbine Division in 1978, where he has since held a variety of positions in new product development, product engineering, and project management.

Mr. Lucas received B.Sc. (1975) and M.Eng. (1976) degrees from Cornell University in Ithaca, New York. He holds two U.S. Patents, and has authored several technical papers on topics including the development of abradable seals for steam turbines, compressed air energy storage, and the development of syn-gas drive steam turbines.

ABSTRACT

The design, analysis, and testing of a high performance steam turbine driver for a critical service synthesis-gas compression train are discussed. The high power, high speed, double end drive and extraction condensing conditions of this type of machine present unique challenges to the rotor and flowpath design. These issues are discussed and test data presented that demonstrate the importance of considering the rotor's dynamic characteristics at the design phase in order to build smoother and more reliable turbomachinery.

INTRODUCTION

Steam turbines first produced useful work well over a century ago. Their reliability, efficiency, and versatility are possibly the three main attributes that have contributed to their widespread utilization in a wide range of applications. Steam turbines can be found driving equipment ranging from generators, compressors, pumps, fans, and mills to the main propulsion units of marine vessels. They are employed in a variety of industries from utility, petrochemical, and mining to pulp and paper. Of the steam turbines employed in these industries, the most sophisticated and consequently challenging design is that which drives a synthesis-gas compressor of the type used in ammonia and methanol plants.

Steam turbines that drive synthesis-gas compressors are required to operate at high speeds with high throttle flows and elevated inlet steam conditions. These turbines have condensing exhausts and often contain a controlled extraction that adds to bearing span and hence rotor flexibility. These features present unique challenges to the rotor and bearing design that must be carefully addressed to assure sound and reliable operation. For example, partial admission steam forces from the inlet and extraction sections can be large enough to affect bearing loading and, therefore, rotor response. Furthermore, the destabilizing forces from steam swirl in the high-pressure labyrinth seals and blade tip clearance leakage can be large enough to drive the rotor unstable. These issues are discussed along with other factors that must be considered in the design of a rotor for a high performance steam turbine.

In the case study presented, the dynamic performance of the rotor was a prime consideration in establishing the main parameters of the design. Rotor geometries, such as bearing span, shaft diameter, wheel and overhung weight, along with the bearing and support structure properties, are parameters that can be varied to tune critical speeds in relation to the operating range and reduce response sensitivity to steam forces. The objective is to produce a design that not only complies with the requirements of any applicable specifications, but also one that has minimal dynamic sensitivity to external operational influences.

Although the rotating component of a high performance steam turbine is reviewed, the analysis methodology presented can be used in the rotordynamics evaluation of all steam turbines. Furthermore, some of the features discussed can be incorporated into other steam turbine designs, as well as other types of turbomachinery.

High Performance Steam Turbines

In large scale petrochemical processes there is a fundamental need to compress gases to increase reaction rates in order to reduce

the size and cost of major components in the system. The required speeds and powers are dictated by the compressor designer, and vary over a wide range depending on the molecular weight, flowrate, and pressure ratio of the gas being compressed. Heat to produce steam typically comes from the process, and steam use is typically divided between a number of turbines and process heating requirements. Capital costs and process economics for the plant lead to moderate demands for thermodynamic economy of the steam turbines.

The ammonia manufacturing process offers some of the more demanding challenges of steam turbine design. Figure 1 illustrates a somewhat dated schematic of this process, and Figure 2 a typical arrangement of the major steam turbines and their operating conditions. Most of the drivers operate on intermediate pressure steam extracted from the primary synthesis-gas compressor driver. This scheme allows the overall system to take advantage of the thermodynamic economy offered by relatively high inlet steam conditions, while not burdening the lower power drivers with its efficiency compromising aspects. On the other hand, the primary driver efficiency benefits from larger inlet flows while the design of the low-pressure section is much relieved by extracting 80 percent or more of the flow at the intermediate pressure level.

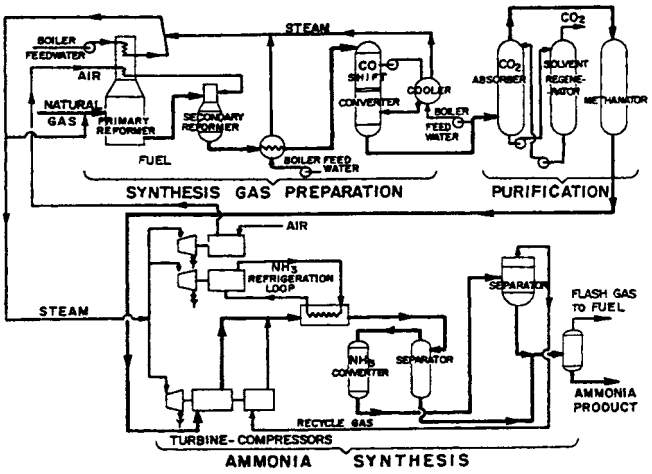

Figure 1. Typical Ammonia Manufacturing Schematic.

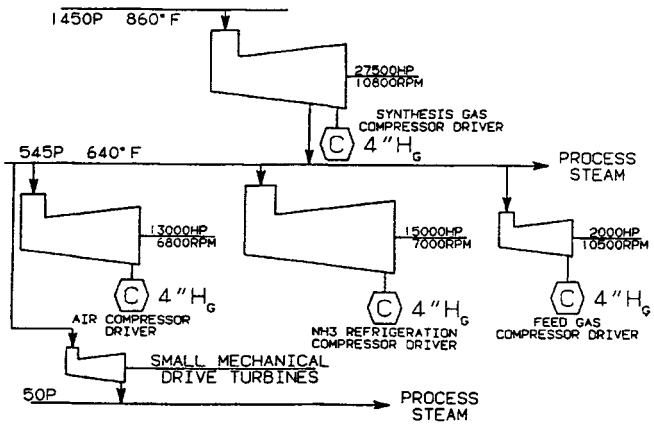

Figure 2. Typical Arrangement of Steam Turbine Drivers in an Ammonia Plant.

Steam turbines that drive synthesis-gas compressors (hereafter called syn-gas turbines) operate with high throttle flows at elevated inlet temperatures and pressures, and produce high power at high rotational speeds. These requirements present unique challenges that, over the years, have culminated in some of the most sophisticated steam turbine designs produced. Even so, in their early stages of development, turbine designers had to employ many different concepts to overcome the then limitations in analytical prediction methods, manufacturing technology, and materials availability.

The modern single casing syn-gas turbine shown in Figure 3 is the culmination of a design evolution stretching over several decades. It was common practice at one time to build syn-gas turbines as two casing designs (Figure 4) with separate high-pressure and low-pressure turbines connected by a crossover duct. The exhaust from the high-pressure turbine supplied flow to meet the process requirements with the remainder going to the low-pressure condensing turbine. At the time this was very effective, since the use of two casings avoided many compromises in both rotor and flowpath design. Each turbine section was relatively short in length, and rotordynamics problems relatively minor and easily dealt with. Moreover, with two relatively short rotors, there were no serious restrictions on flowpath design and hence thermodynamic efficiency.

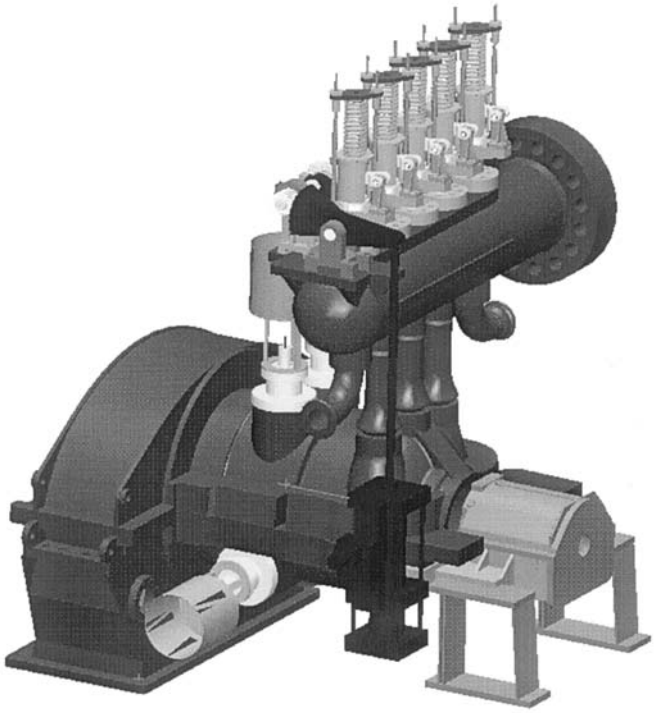

Figure 3. Modern Single Casing Syn-Gas Drive Steam Turbine.

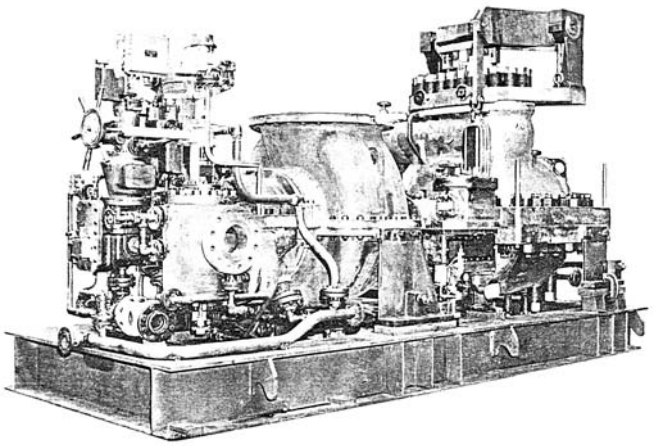

Figure 4. Early Double Casing Syn-Gas Drive Steam Turbine.

Ultimately, simple economics provided the impetus for the development of the single casing syn-gas turbine. Two casing designs were complex and expensive, with duplication of bearing and support systems, two complete casing and rotor systems, an additional coupling, and a crossover duct. In addition to the obvious initial capital cost, many of these extra components required maintenance and periodic replacement. Space requirements and installation complexity were additional factors that eventually provided the incentive for the development of the single casing design. A side benefit of this design was an improvement in overall efficiency due to the elimination of the crossover duct and one set of journal and thrust bearings and associated losses as well as steam leakage. These designs first appeared approximately 30 years ago, and quickly became the industry standard. Over the intervening years, continued refinement and development have yielded significant improvements in thermodynamic efficiency, mechanical reliability, and rotordynamics performance compared to those early designs. Presented herein is the case study of the rotordynamics design, analysis, and verification testing of a modern single casing syn-gas turbine.

SYN-GAS DRIVE STEAM TURBINE

Figure 5 depicts a cross section of a new generation syn-gas turbine typical for both ammonia and methanol processes. The turbine is a single casing design with high-pressure and temperature inlet, a controlled extraction, condensing exhaust, and double extended shaft ends to drive one or more compressors from each end. The basic design of the high-pressure inlet section is capable of operating steam conditions of up to 2000 psig and 1000°F. The overall unit is roughly 11 ft long by 10 ft wide by 12 ft high, and weighs approximately 100,000 lb.

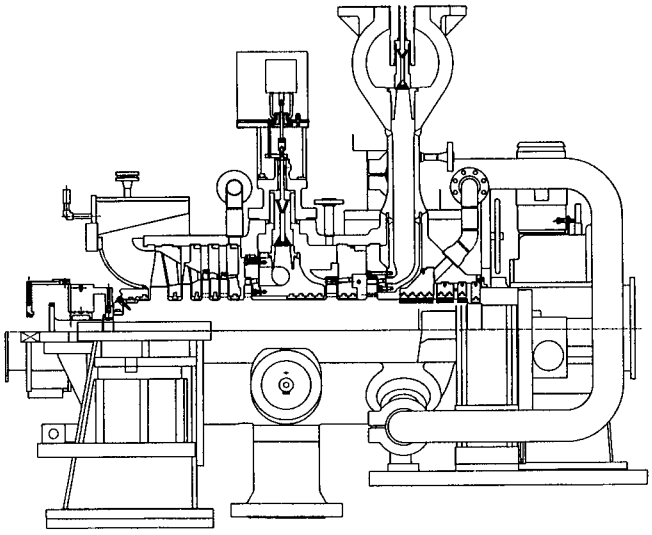

Figure 5. Cross Section of Single Casing, Single Flow Syn-Gas Drive Steam Turbine.

The turbine application of this case study can produce nominally 40,000 hp, and has a design operating speed range from a minimum governor of 8077 rpm to a maximum continuous of 10,601 rpm. The flowpath consists of a two-stage high-pressure head end and a five-stage condensing section as shown in Figure 6, which depicts the rotor in the lower half casing. The high-pressure turbine casing is a composite fabricated from several low alloy and carbon steel castings, while the condensing exhaust casing is a fabrication of carbon steel plate and structural shapes. The entire casing, extraction control section, and exhaust were specifically designed to minimize the overall bearing span to produce a rigid, nonresponsive rotordynamic system. Equally, the flowpath was specially developed to meet the demanding simultaneous requirements of high thermodynamic efficiency and high blading reliability.

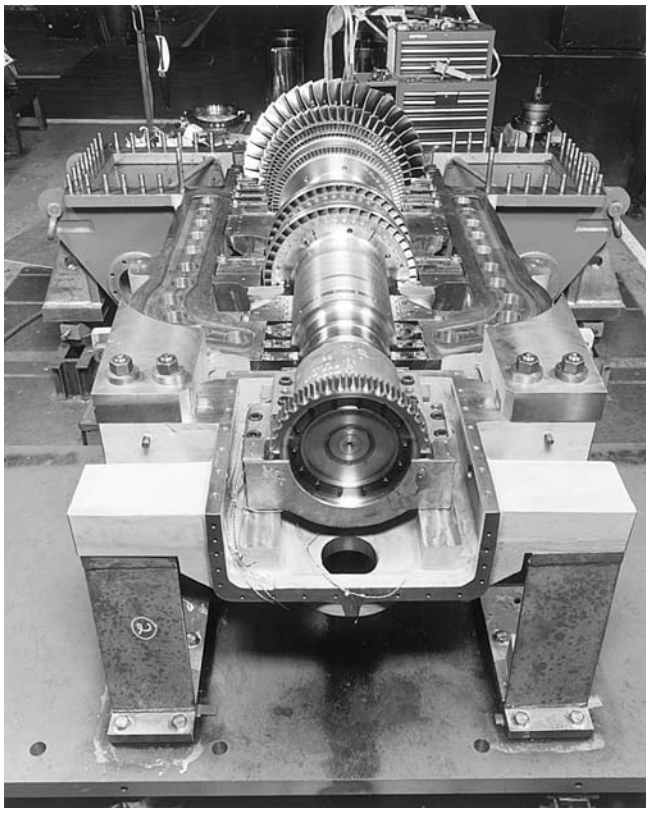

Figure 6. Rotor Supported in Lower Half of Steam Turbine Casing.

High-Pressure Section

Various options were evaluated in depth before the final configuration of the high-pressure section was established. Several factors influenced the final design. Syn-gas processes are somewhat unique in the high rate of extraction required of the turbine. Eighty percent or more of the total steam flow is typically extracted at relatively high pressure. This means that a major portion of the total turbine power is produced in the high-pressure section. Consequently, the thermodynamic efficiency of this section is critical to the success of any syn-gas turbine design.

Motivated by this obvious concern with improving efficiency, an inner barrel style steam end was one of the first options considered. In an inner barrel design, the inlet nozzle passages, nozzle ring, and one or more subsequent stages are contained in a second case supported inside the main turbine casing (Figure 7). Since the inlet and stage pressures are contained inside two casings, each of which sees only a portion of the total pressure, this design is capable of maintaining very high first stage pressure. Consequently, the casing design is very conservative regarding both basic stress levels and sealing. With its high pressure capability, the performance potential with an inner barrel can be optimized with up to a three-stage high-pressure turbine section.

However, an inner barrel design suffers from a few disadvantages. To maintain high first stage pressure, an effective shaft seal at the rotor's penetration of the inner barrel is necessary. This adds significantly to the required shaft length, and leakage through these seals dilutes the performance benefit of the high stage pressure. To truly optimize the efficiency of a three-stage high-pressure design would require a smaller flowpath, and hence shaft diameter, than is desirable for good rotordynamics.

An alternative to the inner barrel, used very successfully on other applications, is the finger type (Figures 8 and 9). In this

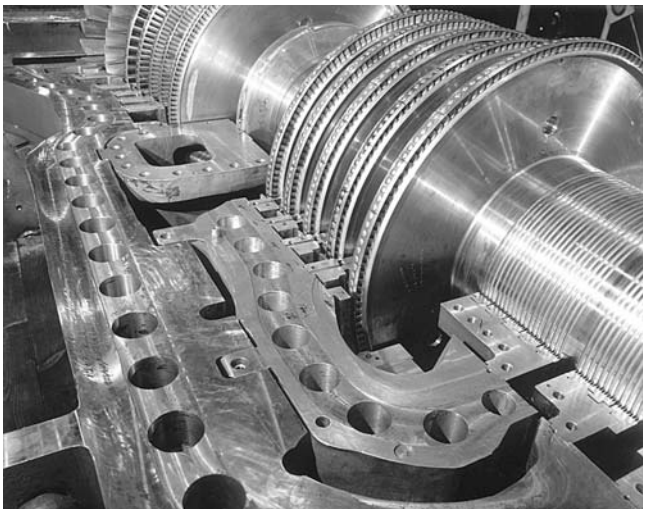

Figure 7. Inner Barrel Supported in Main Turbine Casing.

design, the high-pressure inlet steam is contained by two pressure casings. Inlet steam is conveyed to the nozzle ring by separate nozzle passages (or fingers) suspended inside the outer casing. The pressure contained by the single shell, or main outer casing, is then limited to first stage pressure. A disadvantage of this design, however, is that it has lower first stage pressure capability than with an inner barrel.

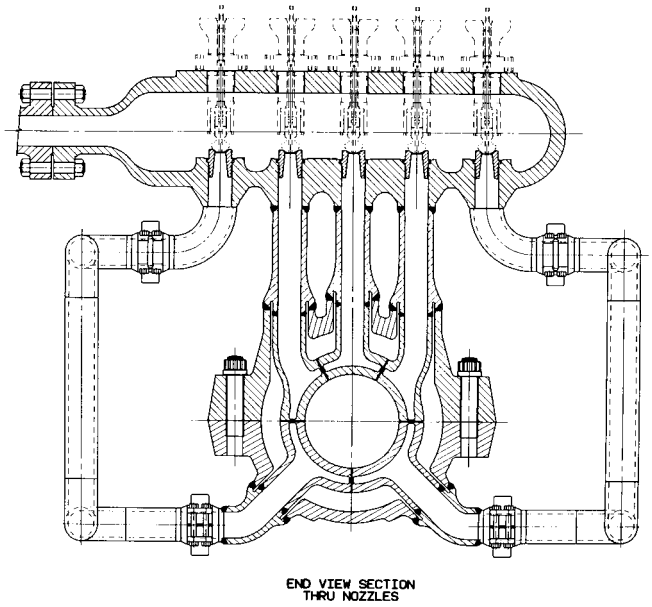

Figure 8. Schematic Showing Finger Passages Suspended Inside Main Turbine Casing.

Nevertheless, the single casing design turns out to be an excellent compromise. By optimizing the high-pressure section as a two-stage design, the resulting larger flowpath diameter permits a correspondingly larger shaft diameter. With elimination of the inner barrel's extra set of shaft seals and associated leakage losses, the performance of the two-stage design approaches that of the three-stage design, but in a much shorter axial space. Since two-thirds of the power is developed in this section, every one percent gain in efficiency equates to two-thirds of a percent increase in overall turbine efficiency. Optimum performance, therefore, must be accomplished through proper selection of the wheel diameter and number of stages.

Figure 9. Nozzle Bowl Passages in Upper Half of Main Casing.

The finger type inlet with a two-stage high-pressure section was ultimately chosen as the optimum for the syn-gas turbine discussed. Axial entry fir tree roots were used on the blades to withstand the high steam bending loads imposed on these stages and integral shrouds with a friction band for additional damping (Figure 10). An additional benefit with axial roots is a more compact wheel design that yields shorter bearing spans compared to the use of more conventional tangential entry roots. Grade 422 stainless steel was used for these blades due to the higher stage temperatures. This configuration resulted in good thermodynamic efficiency, and a combination of axial spacing and shaft diameter that was conducive to excellent rotordynamic characteristics.

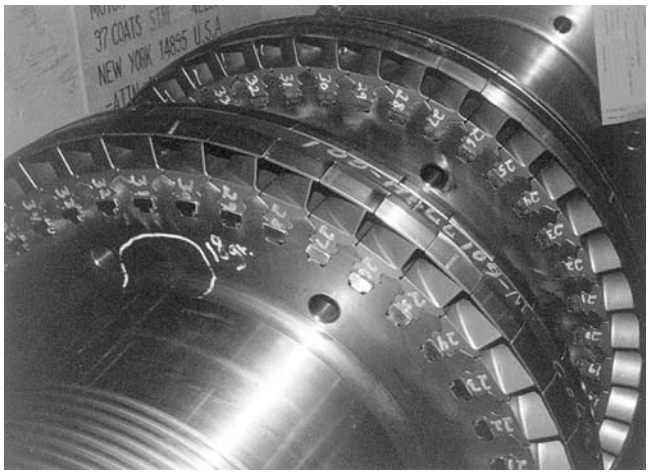

Figure 10. High-Pressure Rotating Blades.

The high-pressure section of the turbine is supported by the inlet end bearing case. This assembly primarily houses the journal and thrust bearings, although it also contains other devices such as the turning gear and control instrumentation. Special care must be taken to ensure that the support structure has high vertical and lateral stiffness, particularly under the journal bearing, for proper control of rotor response behavior. The assembly, however, also has to be flexible enough to allow for the large axial thermal expansion of the turbine casing, which can be as much as 0.375 in. The support arrangement adopted is illustrated in Figure 3. For additional vertical and lateral stiffness under the journal bearing, a double flexible plate is used for the inboard support. The outboard flexible plate is preloaded slightly inboard to provide a self-leveling

mechanism. This works by allowing the front end of the bearing case to rise a predetermined amount as the outboard plate straightens due to the axial growth of the casing. This rise compensates for the larger thermal growth at the inboard support, which is considerably hotter than the outboard support due to heat conduction and radiation from the turbine casing. This configuration was intentionally designed to prevent unequal loading of the active thrust bearing from excessive case pitching exceeding the misalignment capability of the bearing. This condition has been a problem on some earlier designs of syn-gas turbine resulting in excessive and unequal thrust bearing temperatures.

Low-Pressure Section

From the advent of single casing syn-gas turbines, the low-pressure flowpath has been a major concern. High centrifugal loads, a consequence of the high rotational speeds, coupled with the inability to accurately predict the vibration characteristics of long blades, forced designers to opt for relatively short blades in the low-pressure section. Short blades were a virtual necessity to ensure a conservative design.

To provide sufficient annulus area, double flow (Figure 11) and in some cases even triple flow, stage arrangements were used for the low-pressure section. These designs were very successful, and with their reliability made single casing syn-gas turbines feasible. However, the multiflow designs inevitably required a great deal of axial length, and were not very efficient. Compared to the modern single flow exhaust, they suffered markedly from higher leakage losses particularly in the crossover passages inherent in a multiflow arrangement. Finally, and perhaps most significant, the larger axial space requirements severely limited options to improve the performance of the high-pressure section.

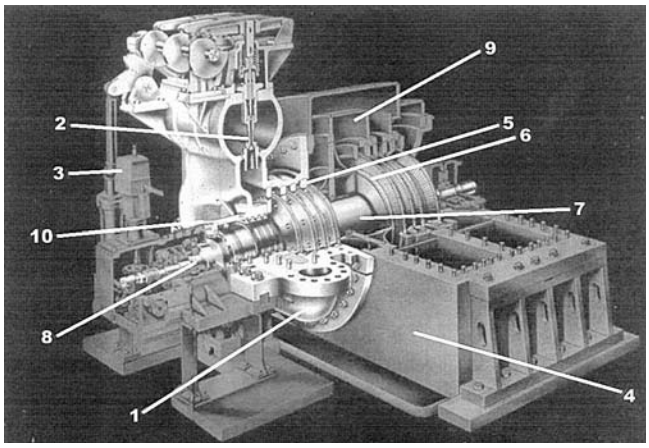

Figure 11. Conceptual Schematic Showing Double Flow Arrangement.

Development of single flow exhaust sections, specifically blades long enough to provide the needed annulus area in a single row, therefore became an essential element in the design of the modern syn-gas turbine. Several unrelated developments, however, first had to come together to make this possible. These included an understanding of the various types of blade failure mechanisms (mechanical integrity and environment) and the conditions initiating them (design, material strength, manufacturing tolerance, and operation (Sohre, 1975)). Second, and perhaps more important, was the development of new and improved analytical techniques. Of these the two that contributed most were the finite element method (not to mention computers powerful enough to make useful analyses practical on a production basis) and improved interference diagrams such as SAFE™ (Singh, et al., 1988), which provided a better understanding and identification of bladed disk vibration.

Another critical development at about the same time was the use of titanium material for the more demanding applications of steam turbine blading. The high strength and low density of titanium allowed designers to take advantage of greatly reduced centrifugal stress levels, while simultaneously permitting higher steam bending loads than competing materials such as stainless steel. An additional benefit was the inherent erosion resistance of titanium, particularly since its primary use is for the low-pressure or condensing blades. In any anticipated syn-gas turbine application, additional erosion protection therefore is not necessary. The final element came with the implementation of computer numerically controlled (CNC) machining capabilities for the economical production of the more sophisticated aerodynamic shapes of these new blades.

In this application, the last two blade rows are freestanding titanium with an axial entry fir tree root design (Figure 12). Unlike the first two rows, however, the root openings in the wheel are not parallel to the axis but rather inclined by an angle of roughly eight degrees to accommodate the airfoil profile at the root. Taken altogether, the development of these sophisticated titanium low-pressure blades was a critical element in the design of the single flow syn-gas turbine.

Figure 12. Low-Pressure Titanium Freestanding Blades.

Although the casing stresses are low in this subatmospheric section, the exhaust end fabrication must be designed so that vacuum deflections are minimal, which otherwise could cause misalignment of the internal parts resulting in operational vibration problems. In addition the support under the journal bearing, which is typically an integral piece of the exhaust fabrication, must be stiff enough in the vertical and lateral directions to ensure proper control of rotor response behavior.

ROTATING COMPONENT

The rotating component comprises a solid single piece integrally forged rotor, with hydrodynamic tilting-pad journal and thrust bearings, and dry type flexible element couplings. Pertinent features are described below.

Rotor Design

For applications up to a maximum stage temperature of 900°F, an ASTM A470 Class 4 rotor material is used. Wheel stresses are limited by design to acceptable levels in order that the Class 4 material can be used since it has significantly better ductility than most alternate materials. When maximum stage temperatures exceed the capability of the Class 4 material, a special differentially heat-treated material developed for high temperature condensing turbines is substituted. This material exhibits ductility similar to Class 4 at low temperatures, but has improved strength in the high temperature section.

As with any engineered steam turbine, first consideration must be given to the design of the flowpath for optimum thermo-dynamic efficiency. This, however, has to be achieved with due regard to the mechanical integrity of the blading from a stress and frequency consideration. In the high-pressure end of a syn-gas turbine, for example, the blades have to be rugged enough to withstand the high temperature of the inlet steam, as well as the high centrifugal and horsepower bending loads acting on these stages.

The rotor design, therefore, is largely dictated by the size of the flowpath, as well as other features such as the size of the inlet, exhaust, and provision for any extraction or induction sections. Thus, the basic rotor geometry, such as the allowable maximum shaft diameter and minimum bearing span, is well established long before any dynamics evaluation can be performed.

The flowpath design and high rotational speed of a syn-gas turbine directs the operation to between the second and third modes. The third mode, which is the first purely flexural mode, is the most responsive by far and can limit the maximum allowable operating speed. Thus, due consideration must be given to maximizing the shaft stiffness while minimizing the overhung weight. Since, however, the maximum shaft diameter is limited by the flowpath and blading design, particular attention has to be directed toward reducing the overhung weight.

Referring to Figure 13, the inlet end overhung weight was reduced by incorporating a double thrust collar arrangement. The outboard thrust collar is integral with the rotor, and provides a flanged face for a coupling. Sandwiched between the collar and the coupling flange is the driven wheel of a turning gear. This wheel also provides the reference signal for the speed pickups of an electronic governor, and eliminates the need for a separate toothed wheel. The inboard thrust collar is an extended shoulder off the shaft penetrating the bearing case. Axial position probes were also included that read off the outboard face of the turning gear/speed pickup wheel. At the exhaust end, the end gland packing case was tucked inside the diffuser to reduce overhung weight as shown in Figure 5. This also moved the centerline of the bearing further inboard, thus eliminating extraneous span. The coupling flange was left integral, with a shaft riding grounding brush located between it and the bearing.

The end result was a rotor with an overall length of 111.3 in, bearing span of 96.0 in, and midspan diameter of 13.0 in. For increased shaft stiffness through both overhangs, the diameter established for both journal bearings was 5.0 in. Radial shaft vibration probes were provided inboard of each journal bearing, 45 degrees either side of top dead center. Two externally accessible field trim balance planes were also included, one located near each end of the central shaft section. This design also has provision for a third plane near the rotor's midspan, adjacent to the downstream face of the wheel immediately upstream of the extraction section.

Bearing Design

Tilting-pad journal and thrust bearings are almost exclusively used in modern high speed turbomachinery. Compared to the fixed geometry sleeve type, tilting-pad journal bearings have excellent stiffness and damping properties that reduce a rotor's sensitivity to unbalanced forces, and far superior stability characteristics at high speeds. Offset-pivoted, self-equalizing tilting-pad thrust bearings are used for their excellent load sharing and load

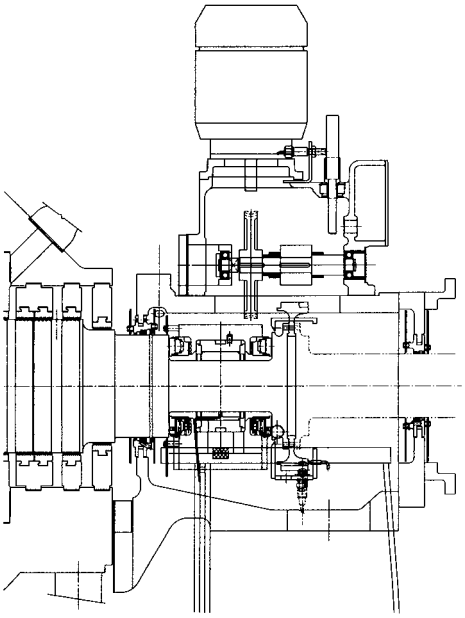

Figure 13. Inlet End Arrangement Showing Shaft Overhang Proportions.

carrying characteristics. Two disadvantages of tilting-pad bearings, however, are the escalating oil film temperatures and frictional losses at high speeds as operation extends into the turbulent regime (Mikula and Gregory, 1981; Edney, 1995).

Over the past decade or so, these issues have been addressed with the development of directed lubrication technology. These new designs provide increased load carrying capacity and reduced frictional losses at lower oil flowrates, without increasing the maximum oil film temperature. The operational performances of several directed lubrication journal bearing designs have been studied (Edney and Mellinger, 1997) and today are widely applied in a variety of turbomachinery.

High efficiency leading edge groove tilting-pad journal and thrust bearings were chosen for this application. For synchronous response and stability reasons, the journal bearing selected was a centrally pivoted, four pad design, orientated load between pivot as shown in Figure 14. The pads have integrally crowned pivots that provide axial alignment capability. Fixed open clearance end seals allow the spent hot oil to exit the bearing axially without restriction and contamination of the fresh cool supply oil. Oversize drain slots machined into the bottom of the housing prevent the bearing cavity from partially flooding with associated churning losses.

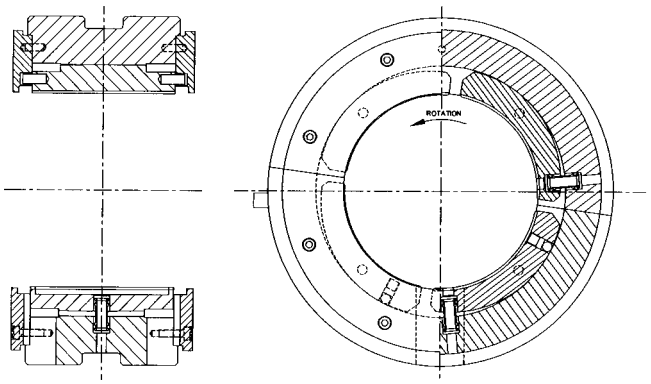

Figure 14. Leading Edge Groove Tilting-Pad Journal Bearing.

Both thrust bearings, illustrated in Figure 15, were a 65 percent offset-pivoted, self-equalizing design with eight shoes per side.

The number of shoes and pivot offset selected were chosen to maximize the load carrying capacity within the available envelope, while maintaining a conservative oil film temperature. The high reaction of the condensing blades used in syn-gas turbines can yield very high axial loads when the turbine is operated without extracting flow. Equally, the high surface speeds of the large bore design dictated by the double end drive arrangement add to the challenge of keeping operating shoe temperatures to acceptable levels. For these reasons, a directed lubrication design is a virtual necessity. Since shoe temperature is the primary concern from an operational standpoint, other options that might be considered to reduce temperature include a 10-shoe design and chrome copper backing material.

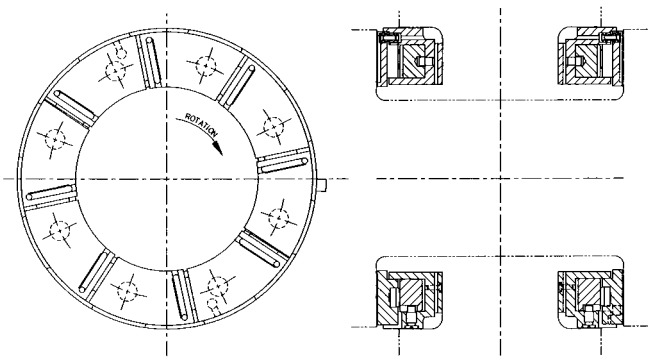

Figure 15. Leading Edge Groove Tilting-Pad Thrust Bearing.

Although the primary reason for using directed lubrication bearings was to address operating temperature, reduced frictional losses and lower oil flowrates were desirable factors also. Temperature sensing instrumentation was in compliance with API 670 (1990).

Bearing Support and Foundation

As already mentioned, the bearing supports should be designed to be as stiff as possible in the lateral and vertical directions between the bearing and foundation for proper control of rotor response. The objective is to optimize the inherent damping within the bearings by maximizing the relative rotor motion at the bearings. This, in turn, increases the effectiveness of the available oil film damping and ultimately minimizes the overall rotor response.

The most common foundation designs are relatively massive reinforced concrete structures that impart a high impedance to the turbine at the connection points. In this respect, they are dynamically similar to most test floor arrangements used during factory tests. Experience has shown that factory tests yield results that are representative of operation in the field.

A case study that describes some of the rotordynamics problems that can occur from inadequate support stiffness is given in Bethel, et al. (1993).

Coupling Design

To minimize overhung weight, integrally coupled, high performance, dry type flexible couplings were specified. These types of couplings do not require lubrication and need little maintenance compared to a gear design (Mancuso, et al., 1989). Also, for a given misalignment, the significantly lower bending moments produced by these couplings help to keep nonessential shaft end stresses to a minimum.

Furthermore, flexible element couplings are extremely accommodating of axial thermal growth, since they can be installed in a prestretched condition. This helps to ensure that, under normal operating conditions, the couplings run in a neutral position thus reducing the overall load on the thrust bearing. This is a very desirable feature on a double end drive machine, such as a syn-gas turbine, where the axial thermal growth at the inlet end can be as much as 0.375 in or more. The coupling specification was in accordance with API 671 (1993).

Rotor Assembly and Balancing

To ensure a well-balanced rotor over the design operating range, a sequential assembly and balance procedure was used. A typical sequence on a solid rotor such as this is to drive the blade rows two at a time starting at the center and working out. The blades should be individually weighed and intentionally arranged so as to minimize the resultant unbalance at each wheel to reduce the amount of grinding or correction weights added. After two wheels have been driven, the rotor should be dynamically balanced across the driven wheels in a low speed balance machine with corrections made only to the driven wheels. This sequence should be followed working toward the shaft ends until all the wheels have been driven. Any shrunk-on components should be added as appropriate in the balance sequence, with corrections made to each component after it is added. This careful and sequential method of assembly and balancing will ensure that a rotor will run from zero to trip speed with minimal levels of vibration.

ROTORDYNAMICS ANALYSIS

The mass elastic model generated of the turbine rotor (Figure 16) is shown in Figure 17. External weights that do not contribute to lateral stiffness (such as the blading, turning gear wheel, and coupling half-weights) are included in the model as indicated by the vertical arrows. The rotor profile of Figure 17 illustrates the rotor stiffness variation assumed through the wheels. At abrupt changes in diameter, such as at the location of a wheel, the effective stiffness diameter follows a more gradual path. The slope of this stiffness path is widely regarded as following a 45 degree line, which is often referred to as the 45 degree rule. Since, however, most rotordynamics analysis programs are based on cylindrical shaft elements, an average diameter is typically used as the effective stiffness diameter.

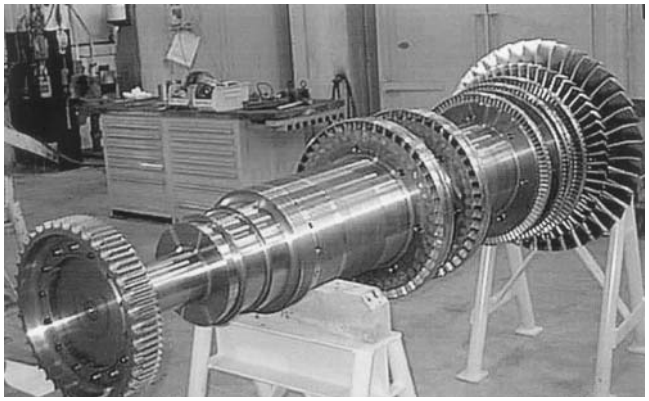

Figure 16. Rotor Viewed from Inlet End.

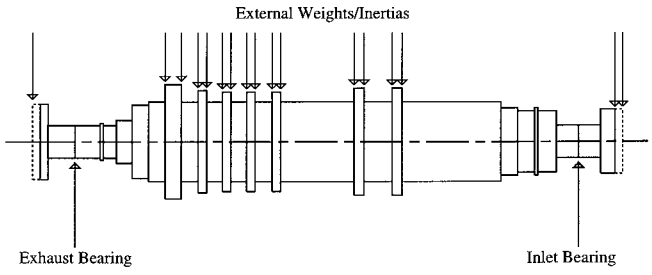

Figure 17. Mass-Elastic Model of Rotor.

The shape and number of elements used to represent the rotor also should be considered carefully. In general, the aspect ratio (length-to-diameter) of each element should not exceed 1.0, and the number used sufficient that adding more would have minimal effect on the results. With today's computing power, there is no reason to economize on the number of elements used to model the rotor. More elements will also yield smoother and more accurate rotor mode and deflected shape response plots.

Support Stiffness

The importance of including the support properties beyond the journal bearing oil film has long been recognized. The total bearing support structure is highly complex, and thus difficult to represent analytically. At the design stage, the determination of accurate values is somewhat nebulous, due to the complex shapes of the support structure, and uncertainties in bolted joints, grout, and other factors. Thus, a simple idealization is often used.

The approach typically used is to include a simple single degree of freedom spring-mass-damper model in series with the oil film. The values used are largely based on experience for a given size of machine and design of bearing case and support. The overall stiffness can be mathematically and/or experimentally approximated from the static deflection of the support structure. Values for the support mass and damping, however, often require additional calculations or approximations. While this approach can be used to adequately predict both the location and amplification factor of a rotor's peak response speeds, it will not yield more than a single support or foundation resonance.

Clearly, simple mathematical models cannot accurately represent the complexity of the various connected structures that exist between the bearings and solid ground. To address this, mechanical impedance test procedures and equipment were developed (Coleman, 1958) to measure the dynamic characteristics of the total support structure at the bearing interface. Two of the earliest applications to rotordynamics analysis in which bearing case supports were experimentally tested to obtain mechanical impedance data are presented in Caruso, et al. (1982), and Barrett, et al. (1986). The experimental data is determined from modal analysis techniques where the response of the structure to a known applied force is recorded. The resulting frequency response function (FRF) data, both magnitude and phase, ideally should be plotted as a function of speed. If the magnitude of the FRF is displacement divided by force, then the resulting data is called a dynamic compliance (Ewins, 1984). One advantage of this method is that the support mass and damping are included implicitly in the FRF along with the support stiffness. These data can then be incorporated into the rotordynamics support model as speed dependent dynamic stiffnesses over the speed range of interest. This information should be obtained to ensure that the support model used in the analysis is adequately representative, and that there are no areas of structural weakness at operating speeds of concern. It may also be required if the unbalance response test data do not correlate well with the analytical model.

The experimental procedure is quite straightforward, and requires either a modal or spectral analyzer. A block diagram of the test arrangement is illustrated in Figure 18. An impact hammer (or shaker) is used to excite the bearing case at the bearing centerline. An internal load cell registers the force imparted by the hammer on the bearing case. Mounted on the bearing case at the centerline is an accelerometer that senses the resultant motion of the bearing case from the impact force. The modal analyzer double integrates the acceleration and divides the resulting displacement by the force. This integration and division are the compliance FRF containing both amplitude and phase information. These data can then be input into the support model used for the forced response analysis. An example of a compliance FRF plot is shown in Figure 19 of the inlet end bearing case. A discussion of the theory and application of this procedure with supporting data can be found in Nicholas, et al. (1986).

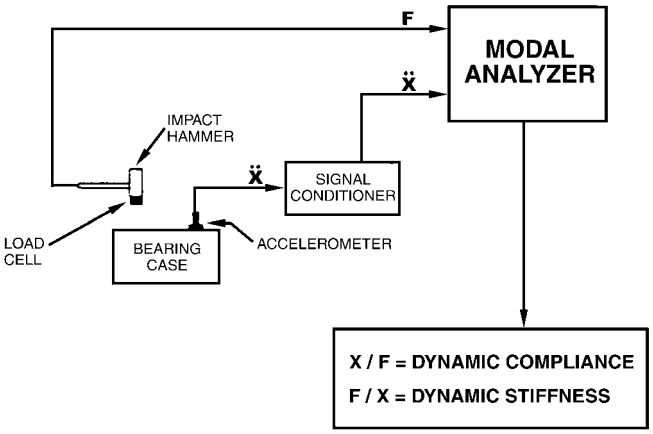

Figure 18. Modal Analysis Schematic Diagram.

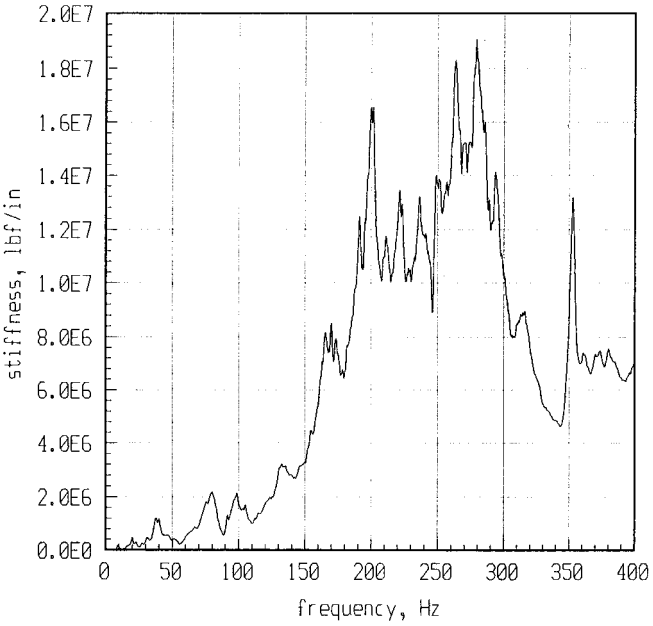

Figure 19. FRF Compliance Plot—Inlet End Vertical.

Undamped Critical Speed Map

An undamped critical speed map is a logarithmic plot of a rotor's lateral undamped resonant speeds versus support stiffness. The term critical speed, however, is often used when referring to the resonant speeds of a rotor as adopted by most industry standard specifications (API 612, 1995). The undamped critical speed map generated for the syn-gas turbine is illustrated in Figure 20 for the first three modes. Critical speeds are approximated by overlaying on this map the speed dependent dynamic stiffnesses of the total support system. This method combines the bearing and support characteristics into an equivalent dynamic stiffness (Caruso, 1958). The inferred critical speeds are clearly very dependent on the curves constructed for dynamic stiffness.

In the absence of any test data, an isotropic single degree of freedom support model was used at both journal bearings. The

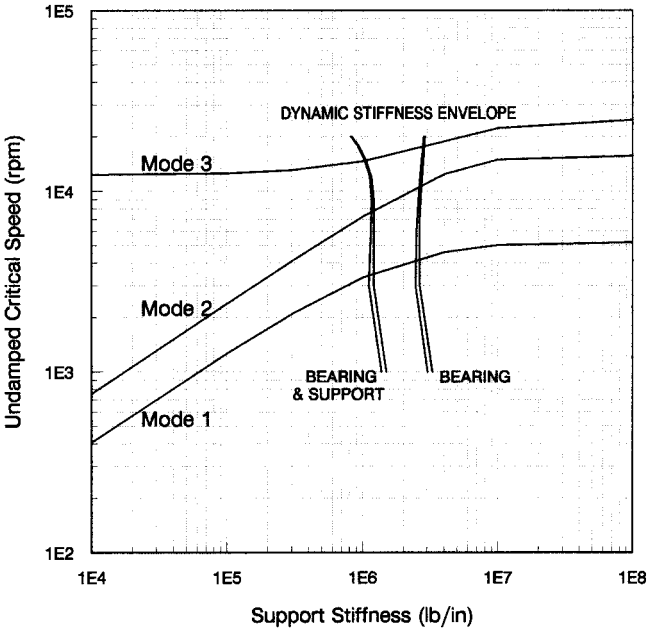

Figure 20. Undamped Critical Speed Map.

stiffness and mass values assumed were based on experience of similar support designs, and the damping 10 percent of critical as in Nicholas and Barrett (1986). Values of 4.0×10^6 lb/in and 500 lb, respectively, were used for the support stiffness and mass at each bearing. The same support model was also used in the unbalance response and stability analyses.

Plotted on Figure 20 are two sets of dynamic stiffness curves. The curve with the higher dynamic stiffness is of the bearing oil film alone. The second curve is of a series combination of the bearing and support. Although the primary determining factor is the bearing oil film, the inherent flexibility of the support structure beyond the bearing must be accounted for to accurately represent the total support system. As can be seen from Figure 20, neglecting the support structure beyond the bearing could lead one to the conclusion that a rotor's critical speeds are higher than actual.

Unbalance Response

An undamped critical speed map provides only a convenient means of quickly assessing the location of modes in relation to the operating speed range. No specific information regarding the severity of the response, however, is available. This is best evaluated by calculating the synchronously forced response to unbalance versus speed. Since the response shape and hence peak location is, to some extent, dependent on the unbalance scheme used, critical speeds identified from these plots are more appropriately referred to as peak response speeds. Guidelines on the amount and location of unbalance that should be used and the acceptance criteria against which the results should be judged are given in most industry standard specifications (API 612, 1995).

First modes are logically excited by a single weight placed at the rotor's midspan. Second modes by two weights, one placed near each end of the central shaft section 180 degrees out-of-phase. Third modes by three weights, one placed at the midspan with the other two at the shaft ends 180 degrees out-of-phase of the central weight. This latter arrangement will ensure that the effect of any shaft end overhung unbalance (such as from the coupling) is accounted for in the determination of peak response speeds. In addition to the response at the bearings, it is normal practice to check all other close clearance points along the rotor for possible rubs from zero to trip.

The results of an unbalance response analysis are given in Figures 21, 22, and 23, for the first three modes. These figures show the predicted synchronous amplitude and phase lag versus speed curves at the following locations: inlet end probes, rotor midspan, and exhaust end probes. For each mode, an arbitrary unbalance of 10 oz-in was used, distributed equally and placed as described above. A single curve only is plotted for each output location, since the response orbits are circular due to the symmetry of the bearing geometry and assumed isotropic support stiffness. The peak response speeds (NC), amplification factors (AF), and peak response amplitudes (A_{max}) at both probe and the midspan locations are summarized in Table 1.

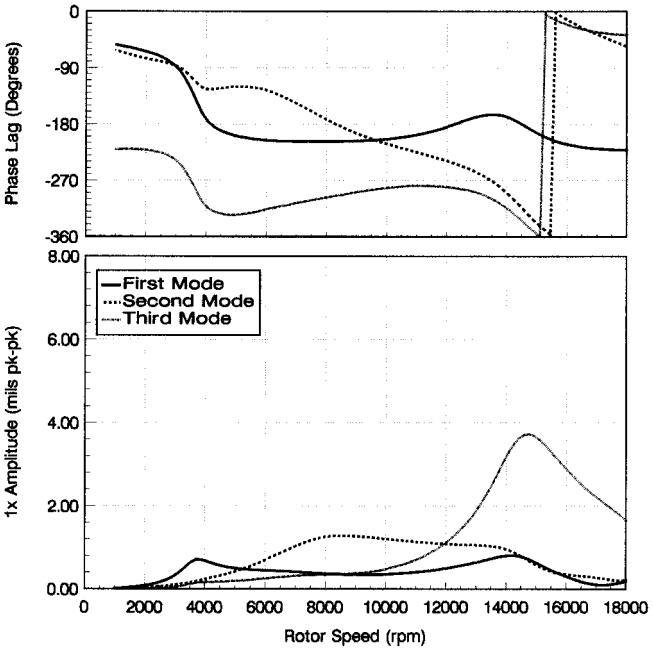

Figure 21. Predicted Amplitude and Phase Lag Versus Speed at Inlet End Probes.

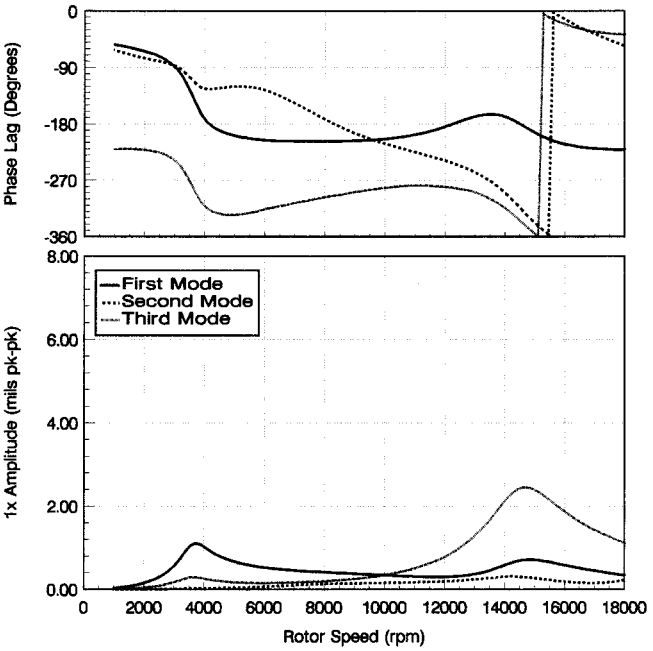

Figure 22. Predicted Amplitude and Phase Lag Versus Speed at Midspan of Rotor.

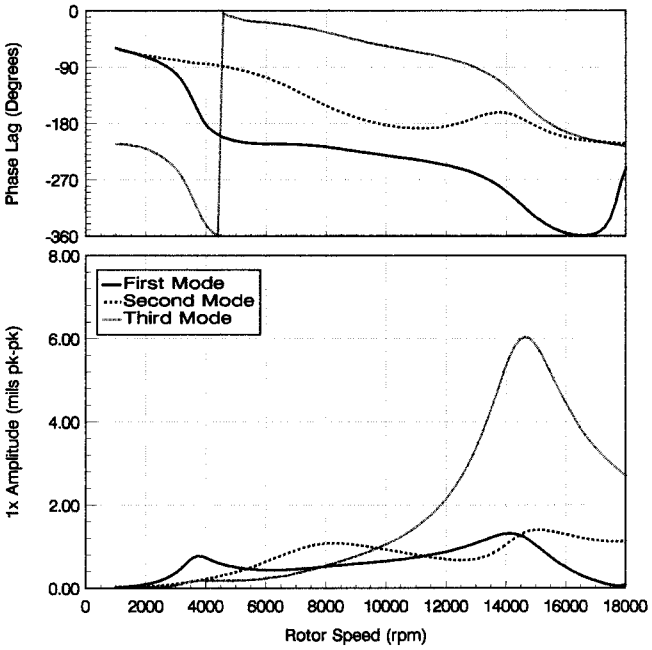

Figure 23. Predicted Amplitude and Phase Lag Versus Speed at Exhaust End Probes.

Table 1. Peak Response Speed, Amplification Factor, and Peak Response Amplitude at Both Probe and Midspan Locations.

MODE	NC (rpm)	AF (dim)	A_{max} (mil pk-pk) IE / MS / EE
First	3750	2.7	0.71 / 1.11 / 0.78
Second	8200	1.7	1.28 / 0.14 / 1.08
Third	14,600	5.4	3.62 / 2.45 / 6.04

The first peak response speed is highly damped, and well below the minimum governor speed. The separation margin comfortably meets the 5.0 percent required by API 612 (paragraph 2.8.2.5b, 1995) for a first mode amplification factor of less than 3.55. The deflected shape is what would classically be described as cylindrical, with the midspan amplitude approximately 50 percent higher than at the probe locations.

At 8000 rpm, the second peak response speed is in the vicinity of the minimum operating speed. However, since this peak response speed has an amplification factor of below 2.5, it is considered to be nonresponsive or critically damped as defined in paragraph 2.8.1.3 of API 612 (1995). No separation margin is required, and operating the turbine on or near this peak response speed is allowed (paragraph 2.8.2.5a, 1995). Operating turbomachinery on or near the second peak response speed in accordance with API specifications has been addressed (Nicholas, 1989). The deflected shape is what would typically be described as conical, with the response at the shaft ends 180 degrees out-of-phase and a nodal situation occurring near the midspan.

The third peak response speed, being the first purely flexural mode, is the most responsive by far. The location of this peak also sets the allowable maximum operating speed in accordance with the API 612 formula for separation margin (paragraph 2.8.2.5d, 1995). The deflected shape has two nodal situations, one near each quarter span location. Of particular interest, however, is that the midspan amplitude is less than at the probes by more than 50 percent. These results illustrate why the excitation of the overhung weight can be important in evaluating third modes. An unbalance at the coupling, for example, could lead to higher response amplitudes at the shaft ends than at the rotor's midspan.

Effect of Rotor Geometry

So why not just lower the second peak response speed comfortably below the operating speed? To some extent, changing the geometry and hence stiffness of a rotor will move the location of peak response speeds. Other factors, such as the bearing and support characteristics, also can be varied to tune the location of peak response speeds. Although such changes might address one mode, they also could adversely affect other modes of concern ultimately degrading the overall rotor response characteristics over the operating speed range.

For example, increasing the shaft stiffness of a relatively stiff rotor while maintaining the same bearing span will raise the location of the third peak response speed, but will have a minimal influence on the locations of the first and second. The magnitude of the response to unbalance will change, however, due to the additional weight supported by the bearings and associated changes in oil film stiffness and damping. Thus, the complete rotorbearing system must be considered when tuning peak response speeds in relation to the operating range.

The effect of rotor geometry is illustrated in Table 2 for the same unbalance schemes used in the baseline example. Illustrated is the effect of a 6.0 in increase and decrease in bearing span, and a 2.0 in increase in shaft diameter. These results are again compared in terms of peak response speed, amplification factor, and peak response amplitude.

Table 2. Peak Response Speed, Amplification Factor, and Peak Response Amplitude for First, Second, and Third Mode Response.

First Mode Response			
	NC_1 (rpm)	AF_1 (dim)	A_{max} (mil pk-pk) IE / MS / EE
6 in Span Increase	3600	3.1	0.73 / 1.22 / 0.78
6 in Span Decrease	3950	2.2	0.72 / 1.03 / 0.78
2 in Diameter Increase	3750	2.9	0.67 / 0.93 / 0.71
Second Mode Response			
	NC_2 (rpm)	AF_2 (dim)	A_{max} (mil pk-pk) IE / MS / EE
6 in Span Increase	8000	1.8	1.31 / 0.13 / 1.12
6 in Span Decrease	8500	1.7	1.25 / 0.10 / 1.06
2 in Diameter Increase	8100	1.9	1.25 / 0.16 / 1.10
Third Mode Response			
	NC_3 (rpm)	AF_3 (dim)	A_{max} (mil pk-pk) IE / MS / EE
6 in Span Increase	14,100	4.9	3.67 / 2.13 / 5.43
6 in Span Decrease	15,100	6.3	3.59 / 2.96 / 6.86
2 in Diameter Increase	15,800	8.0	4.08 / 2.91 / 7.82

The third mode is clearly the most affected by changes in rotor geometry. There is, however, a limit regarding how much the bearing span can be shortened or the shaft diameter increased in an attempt to raise the third peak response for higher speed applications. For example, shortening the span will compress the flowpath, thus adversely affecting the efficiency. Similarly, increasing the shaft diameter will increase the interstage and end gland leakage with associated efficiency and operational stability ramifications. Furthermore, these changes also will likely raise the third mode amplification factor and peak response amplitudes, thus negating some of the increase in separation margin gained versus that required.

In contrast, the first and second peak response speeds are much less sensitive to these moderate changes in rotor geometry. This is of particular interest regarding the second, since it cannot be lowered significantly by geometry changes alone. Other factors would have

to be addressed, such as reducing the bearing stiffness, although there is a limit on how much of a reduction could be achieved. Moreover, these changes would also lower the third peak response speed, which likely would be the limiting factor from a dynamics consideration. It can be seen then that there is a limit on how much the second peak response speed can be lowered (if at all in some cases) below the minimum governor speed of this type of machine, without increasing the sensitivity to unbalance at operating speed.

Thus, for optimum thermodynamic efficiency and rotordynamic performance, an extraction-condensing syn-gas turbine of this type when operating near the low end of its speed range will be in the neighborhood of the second peak response speed. The key is to ensure that the mode is well damped, and insensitive to external operational influences. Nevertheless, these limited results demonstrate some of the rotor geometry changes that can be evaluated in an attempt to tune a rotor's dynamic characteristics in relation to the operating speed range.

Rotor Stability

Rotor stability continues to be one of the primary concerns in rotating machinery operating at high speeds and pressures. An unstable condition will occur when the system destabilizing forces are greater than the restoring damping or stabilizing forces. Destabilizing forces typically arise from oil film sleeve bearings and seals, friction in shrink-fitted components, and aerodynamic excitation. In steam turbines, aerodynamic sources are typically the labyrinth seals and blade tip clearance leakage.

The prevailing method used in the evaluation of rotor stability is to calculate the damped eigenvalues and associated logarithmic decrements. The imaginary part of the eigenvalue is the damped natural frequency, while the real part is the growth exponent. A positive growth exponent is indicative of an unstable system, and a negative value of a stable system. However, for practical reasons, it is more appropriate to convert the growth exponent into a logarithmic decrement. The logarithmic decrement is defined as the natural logarithm of the ratio of two successive amplitudes of a freely oscillating system, and gives a measure of the system damping, or rate of vibration growth or decay, following a disturbing influence. Stability is assured with a positive value for logarithmic decrement; the higher the value the more stable the system. When neglecting aerodynamic forces, a good rule of thumb is that the logarithmic decrement at the maximum operating speed should be greater than 0.3 for assured stable operation.

Typical results are plotted on the whirl speed map of Figure 24, and do not include any destabilizing forces. Illustrated is the effect of rotor speed on the damped natural frequency and logarithmic decrement of the first three whirl modes. Intersection of the whirl speed curves with the synchronous response line gives the approximate location of the first three damped critical speeds. The values for logarithmic decrement noted in Figure 24, being greater than 0.3, are clearly indicative of a highly stable system over the range of shaft speeds plotted.

Aerodynamic Cross-Coupling

High-speed, high-pressure, steam turbines can be prone to self-excited vibration due to the flow of steam through peripheral clearances. The forces that cause these instabilities are often referred to as aerodynamic since they are the result of fluid forces acting on the rotor. In steam turbines there are two sources of concern: labyrinth shaft seals and blade tip clearance leakage.

Labyrinth shaft seals are the primary source of aerodynamic excitation. The magnitude of the destabilizing force, and hence the likelihood of unstable operation, increases with pressure, speed, and rotor eccentricity. The destabilizing forces are a resultant combination of the axial flow associated with the pressure drop across the seal plus the accompanying fluid circumferential velocity due to shaft rotation. The axial component can be more easily explained by considering a stationary rotor. As the rotor eccentricity increases, a larger average pressure develops on the side of the seal with the smaller local

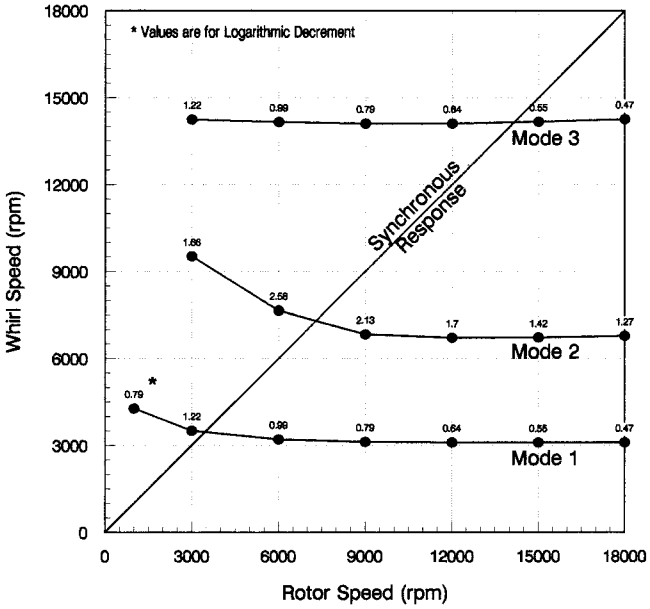

Figure 24. Whirl Speed and Logarithmic Decrement Versus Rotor Speed.

clearance and vice versa. The resultant pressure differential produces a restoring force that opposes the rotor displacement and acts to restore the rotor to the center of the seal, which can be represented as a direct stiffness. When the rotor starts to spin, the fluid forces acting on it become more complicated as illustrated in Figure 25 for clockwise rotation. As the rotor eccentricity increases the clearance cavity becomes progressively more convergent divergent. Similar to a sleeve bearing, hydrodynamic effects cause an increase in pressure in the converging region of the clearance area and a reduction in pressure in the diverging region. This pressure differential yields a net force, Ft, tangential to the rotor's displacement or, as illustrated for the case in Figure 25, to the right in a clockwise (or forward whirl) direction around the center of the seal. The radial force component, $F_r = (K + c\omega)e$, is negligible for labyrinth seals. The tangential force component, $F_t = (k - C\omega)e$, will either destabilize ($F_t > 0$) or stabilize ($F_t < 0$) a rotor in forward whirl. This condition propagates in a self-excited manner producing forces that push the rotor to even higher vibration levels. The complete seal force model can be conveniently expressed in terms of linearized stiffness and damping coefficients as shown by the following equation (neglecting inertia terms that are considered small for compressible flow seals):

$$-\begin{bmatrix} F_x \\ F_y \end{bmatrix} = \begin{bmatrix} K & k \\ -k & K \end{bmatrix} \begin{Bmatrix} x \\ y \end{Bmatrix} + \begin{bmatrix} C & c \\ -c & C \end{bmatrix} \begin{Bmatrix} \dot{x} \\ \dot{y} \end{Bmatrix} \quad (1)$$

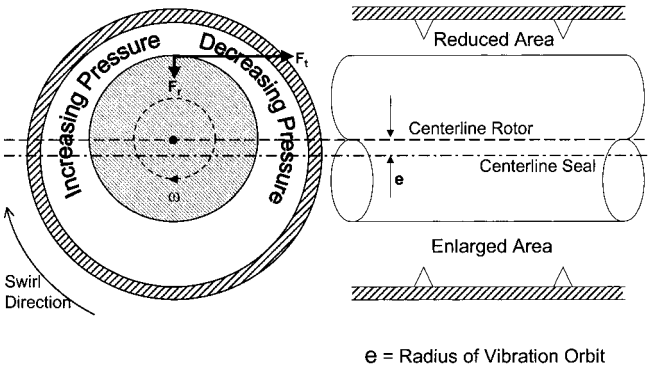

Figure 25. Aerodynamic Seal Forces.

The stability of a seal is largely dependent on the relative magnitudes of the two primary terms; the destabilizing cross coupled stiffness k and the stabilizing direct damping C. Because of its destabilizing influence, the cross coupled stiffness k is the most important of all the coefficients. The second most important, although in general the values are typically low, is the direct damping C since positive values will counteract k. Nevertheless, there are reported cases of the measurement of negative direct damping that would have a destabilizing influence (Kurohashi, et al., 1980). The direct stiffness K is generally quite low and tends to have a small influence on rotordynamics response and stability. Due to the inherent uncertainty in the prediction of these coefficients, as a general rule of thumb a conservative stability analysis would include only the destabilizing cross coupled stiffness values. This approach of ignoring the direct damping C, however, could lead to a somewhat pessimistic conclusion regarding the stability of a rotor system and so should be exercised with some caution. Further, if negative values of direct damping are calculated, then they must be included in the stability analysis to properly account for the destabilizing influence. The quantitative prediction of labyrinth seal force coefficients has been the subject of significant research over the last two decades, and will continue to be so for the foreseeable future.

A secondary aerodynamic source is from tip clearance leakage of the rotating blades in eccentric operation. Thomas (1958) first postulated this phenomenon in connection with instability problems on steam turbines. Alford (1965) later identified the same mechanism associated with instability problems on aircraft gas turbines. In steam turbines these forces are usually neglected due to their relatively small magnitude compared to the labyrinth seal forces. Nevertheless, they can be approximated using the following formula (Thomas, 1958):

$$K_q = \frac{63025\, HP\, \beta}{D_p\, h\, N} \tag{2}$$

where β is an empirical adjustment factor in the range 1.0 to 1.6, and represented through the following force equation:

$$-\begin{bmatrix} F_x \\ F_y \end{bmatrix} = \begin{bmatrix} 0 & K_q \\ -K_q & 0 \end{bmatrix} \begin{Bmatrix} x \\ y \end{Bmatrix} \tag{3}$$

The clearance excitation force is purely destabilizing without any direct stiffness or damping. For the interested reader, the experimental work of Urlichs (1976) on unshrouded, and Leie and Thomas (1980) on shrouded tip leakage effects is suggested. Although these researchers have measured values for β of up to five, experience has shown that for practical purposes a value of 1.0 yields more appropriate results.

The resultant of all the destabilizing forces is opposed by the restoring damping of the hydrodynamic bearings. For this reason, tilting-pad designs are used due to their superior damping and inherent stability characteristics compared to sleeve types. Nevertheless, if the resultant destabilizing force is greater than the overall damping, then large unbounded self-excited subsynchronous vibrations will occur. These vibrations typically appear at a frequency approximately equal to the fundamental lateral natural frequency of the rotor (Greathead and Bostow, 1976). There are exceptions, however, such as the case history presented by Haq, et al. (1998), of synchronous vibration instability associated with a damaged labyrinth seal.

For more information on the prediction and effect of seal and tip clearance forces including current research efforts, Childs' (1993) book and past Turbomachinery Symposium tutorials by Scharrer and Pelletti (1995) and Childs and Vance (1997) are recommended.

The operating conditions of a syn-gas turbine place it in the category of machine that is prone to instability. The effect of aerodynamic cross coupling on the syn-gas rotor is illustrated in Figure 26. Presented are the logarithmic decrements of the first two whirl modes. The destabilizing forces included are the cross coupled stiffness values from the high-pressure end gland and interstage labyrinth seals, and blade tip leakage. Speed dependent coefficients were used in the analysis for the purpose of illustrating their effect. Typical values at the guarantee point are given in Table 3 for reference. The values used were doubled from those calculated to allow for the uncertainty inherent in the prediction of these forces. The computer program used to calculate the seal forces was written by Williams and Flack (1993) and is based on the Childs and Scharrer (1986) adaptation of the method proposed by Iwatsubo (1980). The blade tip leakage forces were calculated using Thomas' formula with $\beta = 1.0$.

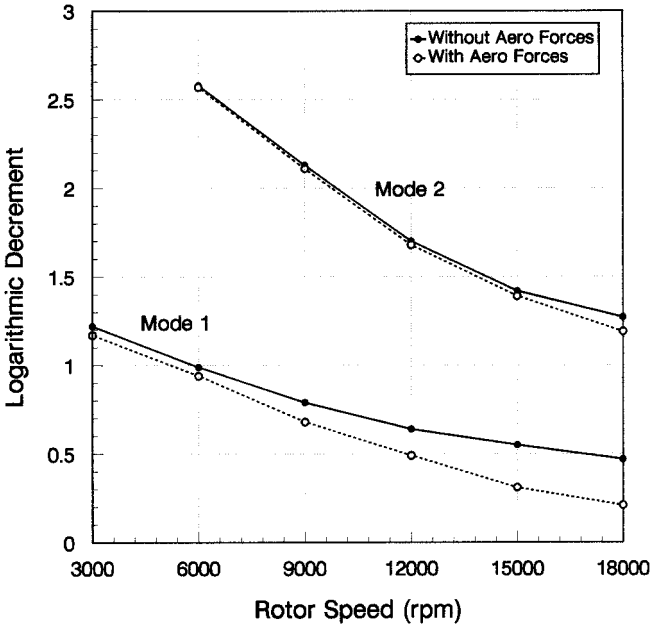

Figure 26. Logarithmic Decrement Versus Rotor Speed with Aerodynamic Cross-Coupling.

Table 3. Aerodynamic Cross-Coupled Forces—Guarantee Point.

Seal Forces		Blade Loading	
Location	Force (lb/in)	Location	Force (lb/in)
HP End Gland	9849	1st Row	3061
2nd Stage	3652	2nd Row	6420
3rd Stage	3361	3rd Row	608
4th Stage	1555	4th Row	1707
5th Stage	1297	5th Row	976
6th Stage	1064	6th Row	253
7th Stage	873	7th Row	134

The general rule of thumb is that with aerodynamic excitation, the logarithmic decrement at the maximum operating speed should be greater than 0.1. In this example, the fundamental mode is clearly the one most affected, although the values noted (Figure 26) are still indicative of a highly stable system. The second and higher modes are largely insensitive to aerodynamic loading, yielding only small reductions in logarithmic decrement. Although not shown, the effect on the whirl speed frequency is minimal, with a difference of less than 5 rpm in each case.

Partial Admission Steam Forces

It has long been recognized that the entire control valve opening sequence and the effect of partial admission diaphragm stages must

be considered in a rotor response analysis. This is especially so in cases where the partial admission forces are large relative to the rotor weight (Pollman and Termuehlen, 1975). The resultant effect can be one in which the rotor is loaded into a sector of the bearing where the dynamic characteristics are significantly different from what they would be due to gravity load alone (Figure 27). Consequently, changes in turbine load can yield significantly different operating vibration amplitudes (Caruso, et al., 1982). This phenomenon, however, cannot be reproduced during a factory solo spin test, since no load is applied to the turbine. Therefore, in cases where the rotor's peak response speeds are close to the operating range, it is good practice to consider their influence at the design stage through analytical simulation.

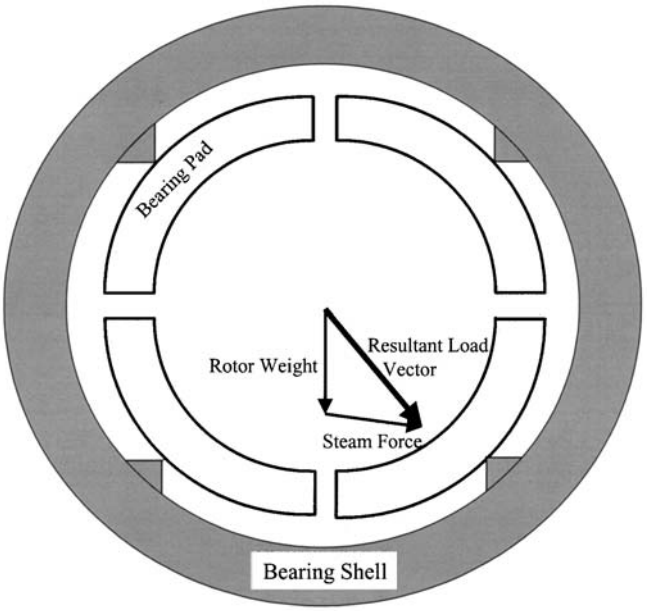

Figure 27. Typical Resultant Bearing Load Vector Due to the Effect of Partial Admission Steam Forces.

There are two sources of partial admission force that result in additional bearing loads. The primary source is the inlet and extraction (if included) control stages, which, depending on the operating point, can have a wide range of admission arcs and hence loading conditions. Another source is partial admission diaphragm stages that are occasionally used for flowpath efficiency considerations. The resultant forces imposed on the rotor are of two types; a tangential component derived from the stage torque reaction, and an axial thrust from the pressure drop across the nozzles. The axial thrust is oriented at the centroid of the admission arc and resolved into radial force couples at the bearings. Nevertheless, the axial thrust forces are usually small compared to the tangential torque reactions and are typically neglected. A possible situation where they might need to be accounted for, however, would be at the inlet control stage with only one or two valves open yielding a small admission arc. Since the pressure drop across the control stage is high, the axial thrust on the first row of blades would also be high and the location of the centroid at a large radius. As the admission arc increases, the radius to the centroid reduces, as does the resultant bearing reaction.

So how do partial admission forces affect the response characteristics of the syn-gas turbine rotor that operates between the second and third peak response speeds? When operating at normal conditions, there is some influence of partial admission loading from both the inlet and extraction control stages. Figure 28 illustrates the determination of the resultant steam forces at the guarantee point, neglecting the axial thrust forces that are small compared to the tangential forces. The steam forces can be resolved into horizontal and vertical reactions at the journal bearings as shown in Figure 29 and summarized in Table 4. The rotor responses with this loading are shown in Figures 30, 31, and 32. The results are summarized in Table 5.

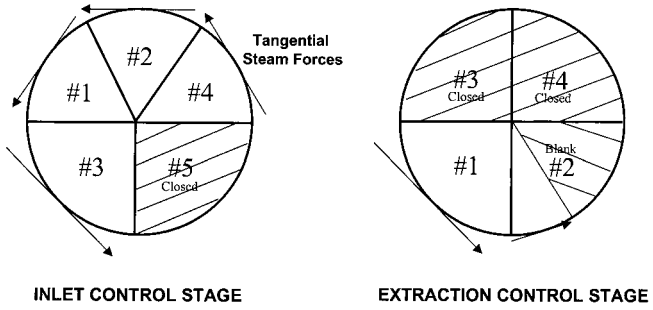

Figure 28. Partial Admission Tangential Steam Forces from Inlet and Extraction Control Stages.

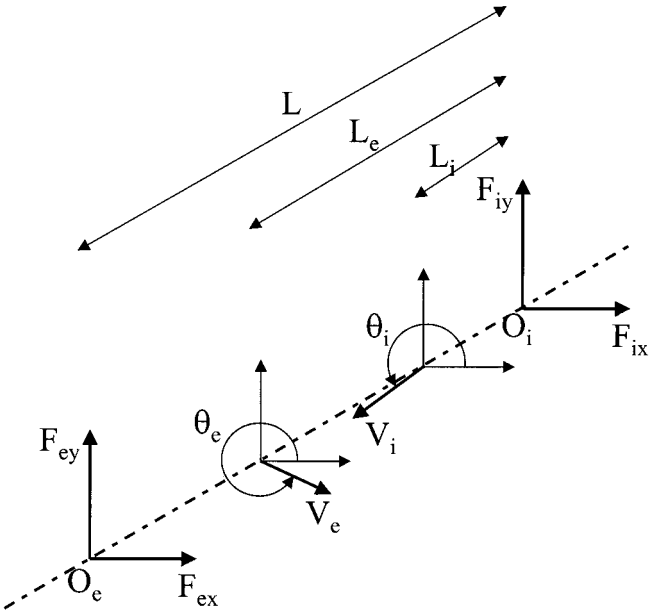

Figure 29. Resolution of Partial Admission Forces into Journal Bearing Reactions.

Table 4. Journal Bearing Loads—Effect of Partial Admission Steam Forces at Guarantee Point.

	Inlet Journal Bearing		Exhaust Journal Bearing	
	F_{ix} (lb)	F_{iy} (lb)	F_{ex} (lb)	F_{ey} (lb)
Without Partial Admission Forces	0	-2017	0	-2196
With Partial Admission Forces	+631	-3126	+204	-3033

It can be seen from the figures that there are now two response curves for each mode. This is because with partial admission, the resultant force vector is not necessarily directed between the two lower half pads, as due to gravity load alone, but is usually at some angle that tends to load one of the pads more than the others. Consequently, the oil film stiffness and damping characteristics change from being highly symmetrical to increasingly more asymmetrical. Correspondingly, the shaft orbits transition from being highly circular and well damped, to increasingly more elliptical and of larger amplitude. Also, a higher resultant bearing load can increase the maximum oil film temperature, which must be taken into account to ensure that the limits of the babbitt are not being approached.

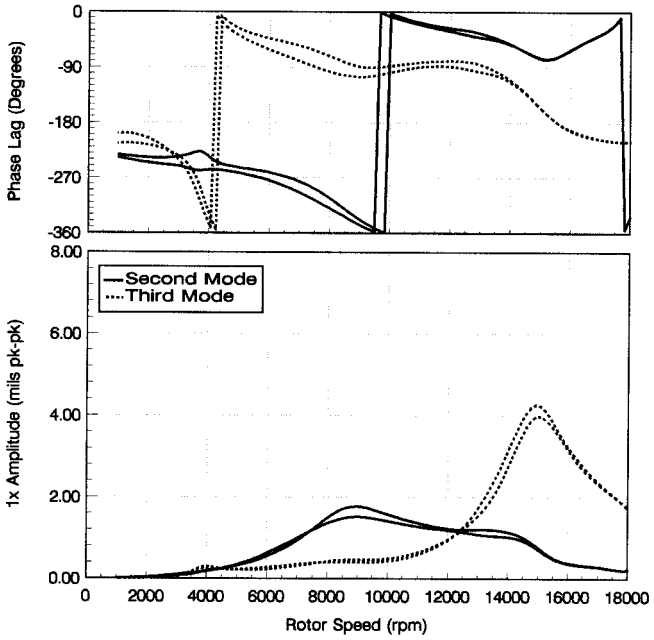

Figure 30. Predicted Amplitude and Phase Lag Versus Speed at Inlet End Probes with Partial Admission Steam Forces.

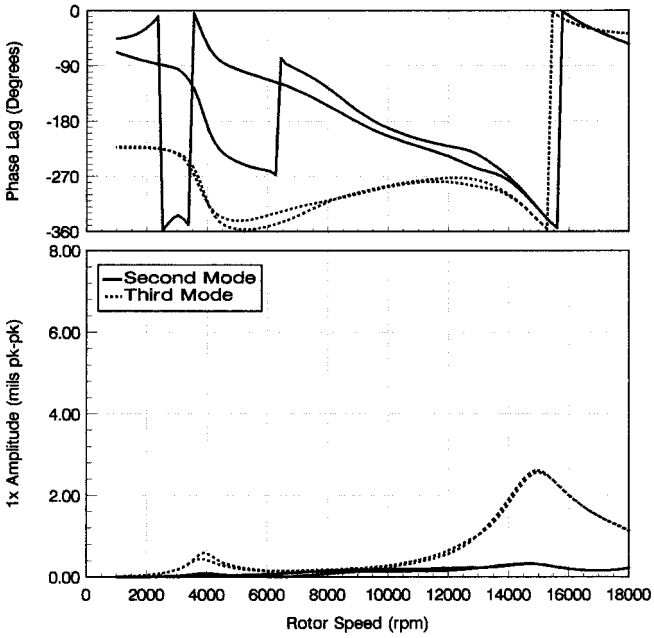

Figure 31. Predicted Amplitude and Phase Lag Versus Speed at Midspan of Rotor with Partial Admission Steam Forces.

In this example, the second mode is slightly more affected than the third. The second peak response speed is higher by 500 rpm, the maximum amplitude greater by almost 50 percent, and the amplification factor increased from 1.7 to 2.3, although it is still indicative of a critically damped response. The third peak response speed is higher by 300 rpm, the maximum amplitude greater by 20 percent, and the amplification factor increased from 5.4 to 6.8. These increases are a consequence of the higher resultant load on the bearing from the steam forces and associated changes in oil film stiffness and damping. It could be argued that the control valve opening sequence could be intentionally arranged so as to reduce the resultant load on the bearings. However, if the resultant load on the journal bearing is virtually negligible, there will be a detrimental effect on stability. This should be avoided.

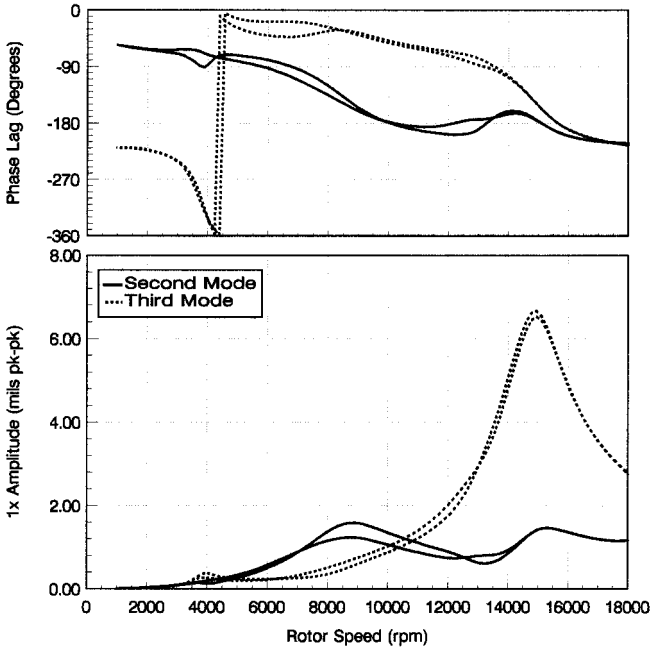

Figure 32. Predicted Amplitude and Phase Lag Versus Speed at Exhaust End Probes with Partial Admission Steam Forces.

Table 5. Effect of Partial Admission Steam Forces on the Second and Third Modes.

MODE	NC (rpm)	AF (dim)	A_{max} (mil pk-pk) IE / MS / EE
Second	8700	2.3	1.77 / 0.18 / 1.60
Third	14,900	6.8	4.30 / 2.60 / 6.70

Comparing the inlet and exhaust end response plots for a second mode unbalance with and without partial admission forces, it can be seen that the vibration magnitude with partial admission is predicted to be higher by up to 50 percent.

A more prudent approach might be to determine the effect on response of opening each control valve successively. By plotting the response amplitude and phase in a vector diagram, an optimum bearing orientation for a given loading cycle can be determined. This approach with supporting data is discussed in Caruso, et al. (1982).

VERIFICATION TESTING

An essential part of a shop test on any piece of rotating equipment is verification of the rotordynamics analysis. This test is performed by deliberately unbalancing the rotor to excite the modes of interest. Steam turbines designed to current rotordynamics specifications (API 612, 1995) are required to have externally accessible trim balance planes for field balancing. These planes also provide convenient locations for deliberately unbalancing a rotor for correlation of the analytical model. On steam turbines, the shop verification test is essentially a no load spin test.

First Mode Verification Test

The first mode verification test was conducted by placing unbalance weights in phase at the trim balance planes. The magnitude of each weight was equivalent to 32W/N, where W is the journal static load nearest each balance plane and N is the maximum continuous speed.

The test results are compared with analytical prediction in Figures 33 and 34. Coastdown data are presented since they do not

include any influence from steam forces. The influence of any residual unbalance inherent in the rotor has been vectorially subtracted out from the data as described by Nicholas, et al. (1997). The results are compared with analytical prediction in Table 6 in terms of the location, amplification factor, and maximum amplitude of the peak response. Although the locations of peak response speed are low by 400 rpm, or roughly 10 percent, the general shape of the response trends is in good agreement. The measured amplification factors are approximately 25 percent high and low at the inlet and exhaust end probes, respectively, and the peak response amplitudes low by up to 35 percent. Response troughs at roughly 9000 rpm also are observed in both the predicted and measured results.

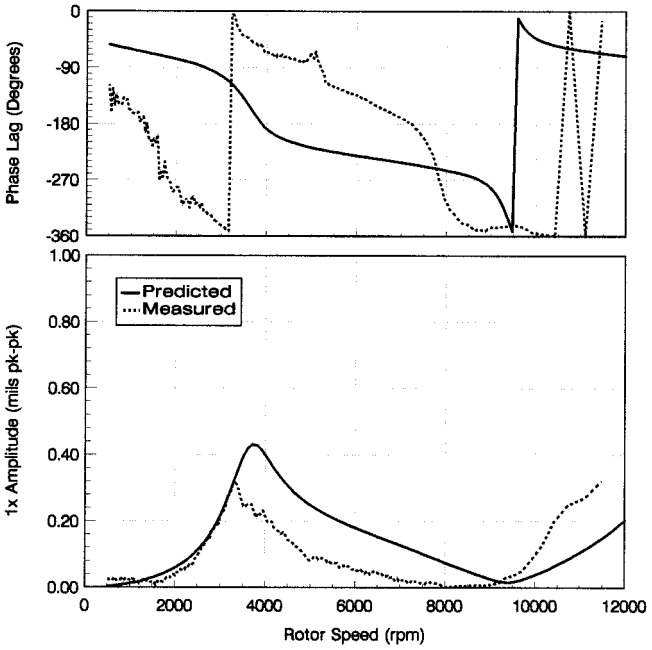

Figure 33. Measured Amplitude and Phase Lag Versus Speed at Inlet End Right Probe—First Mode Unbalance Test.

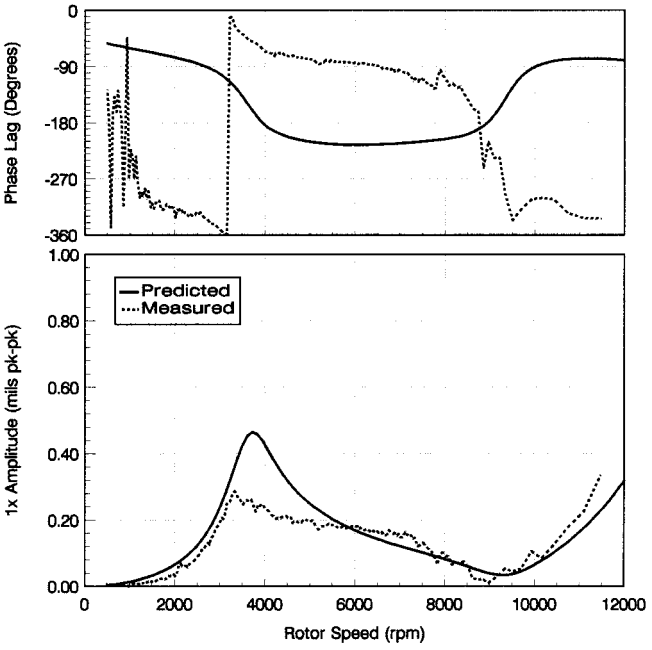

Figure 34. Measured Amplitude and Phase Lag Versus Speed at Exhaust End Right Probe—First Mode Unbalance Test.

Table 6. Measured Versus Predicted First Mode Peak Response—Synchronous Filtered.

	Inlet End Right Probe			Exhaust End Right Probe		
	NC_1 (rpm)	AF_1 (dim)	A_{MAX} (mil pk-pk)	NC_1 (rpm)	AF_1 (dim)	A_{MAX} (mil pk-pk)
Measured	3336	3.6	0.32	3336	2.1	0.29
Predicted	3700	2.8	0.43	3700	2.8	0.46

Second Mode Verification Test

The second mode verification test was conducted using the same unbalance weights as for the first mode, but placed 180 degrees out-of-phase. Coastdown test results with residual subtraction are compared in Figures 35 and 36, and in Table 7 at the peak response. The results are again in good correlation, with the general response shapes in excellent agreement. The difference in location of both peak response speeds is less than 2.5 percent, with critically damped amplification factors.

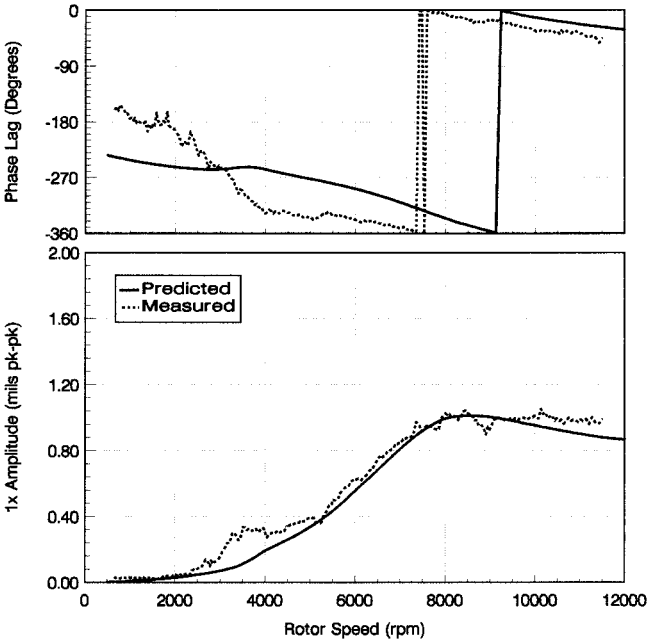

Figure 35. Measured Amplitude and Phase Lag Versus Speed at Inlet End Right Probe—Second Mode Unbalance Test.

As-Balanced Test

Coastdown plots of the rotor as-balanced are given in Figures 37 and 38. Included on the figures are the response trends from both probes at each end of the machine. At the inlet end, the response trends are near equal as would be expected with a four-pad bearing, with the synchronous vibration levels all less than 0.4 mil peak-to-peak from zero to trip. At the exhaust end, however, there is some deviation in vibration magnitude at speeds above 7000 rpm, with the highest level less than 0.5 mil peak-to-peak. This deviation is most likely due to some asymmetry in the stiffness of the support structure. Furthermore, the second mode response as predicted is well damped. There is possibly a slight indication that the third mode response is being approached at the exhaust end, although this peak clearly would be well above trip speed.

Journal and thrust bearing temperature data at the maximum continuous and trip speeds of 10,601 and 11,530 rpm are compared with prediction in Table 8. In this solo or no load test condition, the measured journal pad temperatures are in good agreement with those predicted, with the predicted values consistently higher by up to 5°F. The close agreement between both sets of adjacent pad

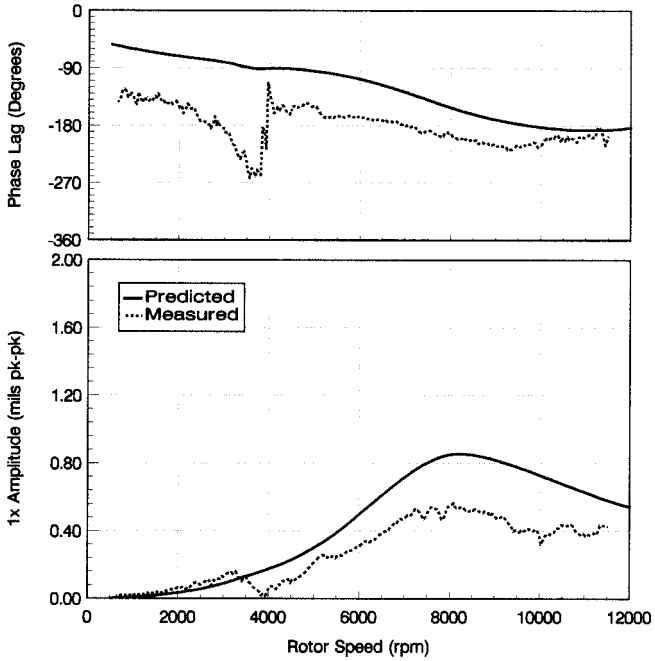

Figure 36. Measured Amplitude and Phase Lag Versus Speed at Exhaust End Right Probe—Second Mode Unbalance Test.

Table 7. Measured Versus Predicted Second Mode Peak Response—Synchronous Filtered.

	Inlet End Right Probe			Exhaust End Right Probe		
	NC_2 (rpm)	AF_2 (dim)	A_{MAX} (mil pk-pk)	NC_2 (rpm)	AF_2 (dim)	A_{MAX} (mil pk-pk)
Measured	8443	-	1.05	8086	2.3	0.57
Predicted	8505	-	1.01	8200	1.7	0.86

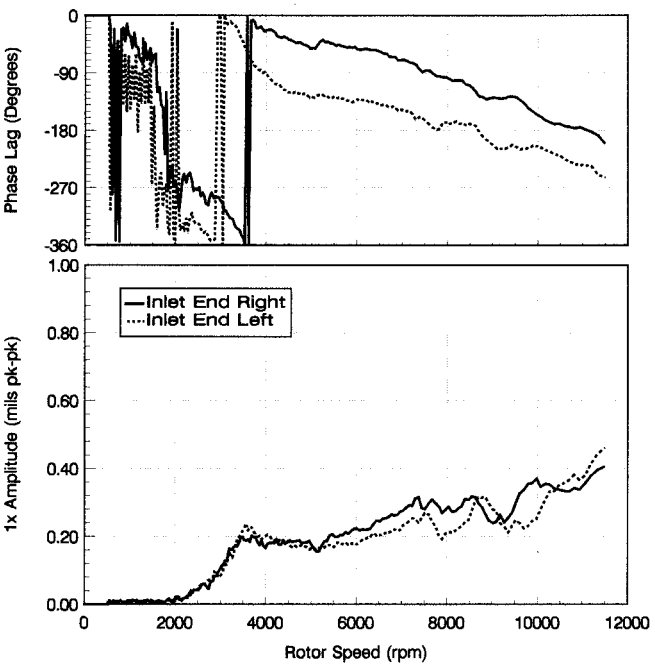

Figure 37. Measured Amplitude and Phase Lag Versus Speed at Inlet End Right Probe—As-Balanced Test.

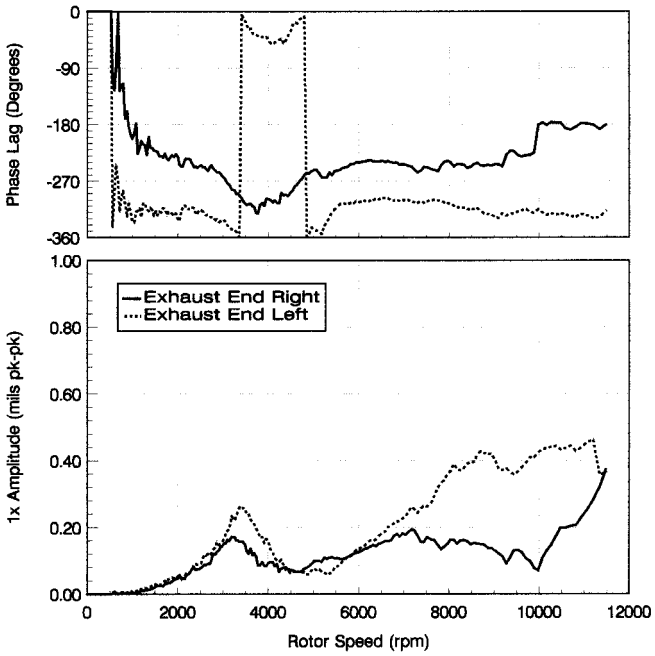

Figure 38. Measured Amplitude and Phase Lag Versus Speed at Exhaust End Right Probe—As-Balanced Test.

temperatures should be expected since in a solo condition the bearing load is directed almost purely between the two lower half pads. The observed difference of less than 5°F in both the predicted and measured temperatures is primarily due to the influence of hot oil carry over on the pad located in the downstream or with rotation location.

Table 8. Shop Versus Predicted Bearing Temperature Data—No Effect of Partial Admission Steam Forces.

Speed (rpm)	Inlet Journal Bearing (Shop / Predicted)		Exhaust Journal Bearing (Shop / Predicted)		Active Side Thrust Bearing (Shop / Predicted)		
	Left (°F)	Right (°F)	Left (°F)	Right (°F)	(°F)	(°F)	(°F)
10601	170 / 171	173 / 176	170 / 173	175 / 178	173 / 172	177 / 172	176 / 172
11530	173 / 175	175 / 180	174 / 177	178 / 181	188 / 183	191 / 183	191 / 183

The measured thrust temperatures are indicative of a well-aligned bearing with the variation between the three instrumented shoes less than 3°F. The measured values although higher, also agree very closely with those predicted. Since there is nominally no load on the thrust bearing in this solo condition, the predicted values were calculated by assuming that the bearing was operating at the mid float position, that is with a pivot film thickness of one-half the total thrust clearance. This assumption is likely the reason for the predicted values being slightly lower than those measured.

The lubricating oil inlet temperature during the shop tests was at 120°F. The predicted bearing temperature values were calculated by the bearing manufacturer (DeCamillo, 2000).

FIELD EXPERIENCE

Operating information from the field is limited to steady-state data. Transient data were not available. Table 9 contains direct unfiltered operating vibration amplitudes at six different speeds. Predicted journal and thrust bearing temperatures are compared with field data in Table 10 at five different operating speeds. The predicted values are calculated at the design operating conditions and include the effects of partial admission steam forces and axial thrust.

Table 9. Field Vibration Amplitudes—Direct Unfiltered.

Speed (rpm)	Inlet End Probes		Exhaust End Probes	
	Left (mil pk-pk)	Right (mil pk-pk)	Left (mil pk-pk)	Right (mil pk-pk)
8077	0.33	0.39	0.43	0.45
8550	0.45	0.49	0.45	0.51
9100	0.54	0.49	0.57	0.52
9206	0.43	0.45	0.49	0.59
9300	0.40	0.42	0.45	0.56
9891	0.61	0.84	0.72	1.02

Table 10. Field Versus Predicted Bearing Temperature Data—Includes Effect of Partial Admission Steam Forces.

Speed (rpm)	Inlet Journal Bearing (Field / Predicted)		Exhaust Journal Bearing (Field / Predicted)		Active Side Thrust Bearing (Field / Predicted)		
	Left (°F)	Right (°F)	Left (°F)	Right (°F)	(°F)	(°F)	(°F)
8550	185 / 174	191 / 188	182 / 175	188 / 184	201 / 211	204 / 211	203 / 211
9100	189 / 176	202 / 190	184 / 177	193 / 186	206 / 214	209 / 214	207 / 214
9206	191 / 176	204 / 190	185 / 178	196 / 187	208 / 215	212 / 215	209 / 215
9300	194 / 177	205 / 191	192 / 178	197 / 187	209 / 216	214 / 216	210 / 216
9891	193 / 179	208 / 193	189 / 181	199 / 189	211 / 220	217 / 220	213 / 220

The difference in the operating vibration amplitude at the two orthogonal probes per end (which are 45 degrees either side of top dead center) is indicative that the response orbit is elliptical. This is consistent with the theory, which predicted that in the presence of partial admission forces the resultant load on each bearing would be directed more heavily on one pad thus yielding asymmetric stiffness and damping coefficients. The fact that the vibration magnitude is higher than observed during the no load factory test also is consistent with theory. For example, in a second mode unbalance condition, the peak response amplitude is predicted to be higher by roughly 38 percent at the inlet probes and 48 percent at the exhaust end probes in the presence of partial admission forces (refer to Tables 1 and 5). Note, in comparing the vibration amplitudes from Table 9 with the response curves in Figures 37 and 38, the values in the table are direct unfiltered and in the figures synchronously filtered.

The journal bearing temperature data are consistent with the vibration trends, with the pad located in the rotation position noticeably hotter than that opposite rotation. Furthermore, the field trends are in fairly good agreement with those predicted in that there is some divergence in temperature between the two loaded pads. This is due to a combination of both a higher resultant load and the influence of hot oil carry over on the pad located in the rotation position. The predicted values, however, are as much as 15°F lower than those measured. This is most likely due to some inaccuracy in the calculation of the partial admission steam forces.

The small difference of less than 6°F between the measured active side thrust temperatures is indicative that under load the bearing is operating well aligned. This implies that the self leveling bearing case also is aligned and operating as designed without any excessive pitching. Furthermore, the measured temperatures are in fairly good agreement with those predicted, being consistently low by 10°F or less.

The lubricating oil inlet temperature in the field is 130°F. The predicted temperature values were again supplied by the bearing manufacturer (DeCamillo, 2000).

SUMMARY AND CONCLUSIONS

The increasing speed and power demands of mechanical drive steam turbines require more sophisticated analytical tools to accurately predict performance. Not least does this include rotordynamics analysis, particularly when applied to machines that are designed to operate on or near lateral peak response speeds. In such cases, the importance of considering external operational influences, such as from steam partial admission and aerodynamic excitation forces as well as support stiffness effects cannot be overlooked.

The case study discussed reviews the rotordynamics analysis methodology employed in the design of a critical service steam turbine driver. Steam turbines that drive synthesis gas compressors are the most sophisticated designs in the industry. The steam turbine reviewed herein was the culmination of a design evolution and field experience stretching over several decades. Computer-aided techniques, extensive shop testing, and improved manufacturing processes were all key factors in producing this state-of-the-art design. In particular, the ongoing refinement and consideration of the rotor's dynamic characteristics from concept to final design resulted in:

- Rotor design in which the API defined critical speeds were placed as far away from the operating range as possible while maintaining efficient staging for the application.
- Highly damped first and critically damped second rotor peak response speeds, with the third well above trip speed.
- Insensitive rotorbearing design with minimal sensitivity to unbalance at the second peak response speed allowing operation on or near it.
- Rotor response characteristics that were carefully tuned in relation to the operating range of the application.
- Integral coupling flange reduced moment shaft end design to minimize response sensitivity to overhung unbalance.
- Optimized bearing performance through the application of high efficiency leading edge groove bearings.
- Consideration of the destabilizing forces of labyrinth seals and blade tip clearance leakage on rotor stability.
- Evaluation of the effect of partial admission steam forces on steady-state bearing performance and rotor response.
- A sequential method of assembly and low speed balancing the rotor to ensure smooth operation at speed from zero to trip.
- Inclusion of two field trim balance planes and a turning gear.

This careful consideration of the rotor's dynamic characteristics throughout the design was confirmed on the test stand as demonstrated by:

- Excellent correlation of the analytical model through first and second mode unbalance testing.
- A critically damped, or nonresponsive, second mode with the third well above trip speed.
- A highly damped lateral rotorbearing design with synchronously filtered vibration levels from zero to trip speed of less than 0.5 mil peak-to-peak.

And verified in the field as demonstrated by:

- Low vibration amplitudes over the normal operating speed range of overall (unfiltered) value less than 1.0 mil peak-to-peak.
- Journal and thrust bearing temperatures in reasonable agreement with predicted values with the turbine operating at load.
- Vibration and journal bearing temperature trends consistent with those predicted in the presence of partial admission steam forces.

NOMENCLATURE

AF = Amplification factor (dim)
A_{max} = Maximum amplitude at NC (mil peak-to-peak)

c = Cross coupled damping coefficient (lb-sec/in)
C = Direct damping coefficient (lb-sec/in)
D_p = Blade pitch diameter (in)
e = Synchronous precession orbit (in)
EE = Exhaust end response
F_{ex} = Exhaust end bearing partial admission steam force reaction X direction (lb)
F_{ey} = Exhaust end bearing partial admission steam force reaction Y direction (lb)
F_{ix} = Inlet end bearing partial admission steam force reaction X direction (lb)
F_{iy} = Inlet end bearing partial admission steam force reaction Y direction (lb)
F_r = Radial force component (lb)
F_t = Tangential force component (lb)
F_x = Force in X direction (lb)
F_y = Force in Y direction (lb)
h = Blade height (in)
HP = Stage horsepower (hp)
IE = Inlet end response
k = Cross coupled stiffness coefficient (lb/in)
K = Direct stiffness coefficient (lb/in)
K_q = Clearance excitation cross coupled stiffness (lb/in)
K_{xy} = Cross coupled stiffness coefficient (lb/in)
K_{yx} = Cross coupled stiffness coefficient (lb/in)
L = Bearing span (in)
L_e = Length from inlet end bearing to extraction control stage (in)
L_i = Length from inlet end bearing to inlet control stage (lb)
MS = Midspan response
N = Shaft speed (rpm)
NC = Peak response speed (rpm)
V_e = Extraction control stage partial admission force vector (lb)
V_i = Inlet control stage partial admission force vector (lb)
β = Empirical adjustment factor, typically assumed to be 1.0 (dim)
θ_e = Angle from X direction to extraction control stage force vector (deg)
θ_i = Angle from X direction to inlet control stage force vector (deg)
ω = Shaft speed (rad/sec)

REFERENCES

Alford, J., 1965, "Protecting Turbomachinery from Self-Excited Rotor Whirl," Transactions of the ASME, Journal of Engineering for Power, *87*.

API Standard 612, 1995, "Special Purpose Steam Turbines for Refinery Services," Fourth Edition, American Petroleum Institute, Washington D.C.

API Standard 670, 1990, "Special Purpose Couplings for Refinery Services," Second Edition, American Petroleum Institute, Washington D.C.

API Standard 671, 1993, "Vibration, Axial Position, and Bearing Temperature Monitoring Systems," Third Edition, American Petroleum Institute, Washington D.C.

Barrett, L. E., Nicholas, J. C., and Dhar, D., 1986, "The Dynamics Analysis of Rotor Bearing Systems Using Experimental Bearing Support Compliance Data," Proceedings of the Fourth International Modal Analysis Conference, Union College, Schenectady, New York.

Bethel, L. L., Gans, B. E., Brown, R. N., and Lewis, R. A., 1993, "Critical Speeds and the Importance of Stiffness—A Case Study in the Design and Testing of a Large Mechanical Drive Steam Turbine to API Standard 612," *Proceedings of the Twenty-Second Turbomachinery Symposium*, Turbomachinery Laboratory, Texas A&M University, College Station, Texas, pp. 73-80.

Caruso, W. J., 1958, "Prediction of Critical Speeds of Steam Turbines by Dynamic Stiffness Method," Colloquial on Mechanical Impedance Methods of Mechanical Vibration, American Society of Mechanical Engineers.

Caruso, W. J., Gans, B. E., and Catlow, W. G., 1982, "Application of Recent Rotor Dynamics Developments to Mechanical Drive Turbines," *Proceedings of the Eleventh Turbomachinery Symposium*, Turbomachinery Laboratory, Texas A&M University, College Station, Texas, pp. 1-18.

Childs, D. W., 1993, *Turbomachinery Rotordynamics—Phenomena, Modeling, and Analysis*, New York, New York: John Wiley and Sons, Inc.

Childs, D. W. and Scharrer, J. K., 1986, "Experimental Rotordynamic Coefficient Results for Teeth-on-Rotor and Teeth-on-Stator Labyrinth Gas Seals," Transactions of the AMSE, Journal of Engineering for Gas Turbines and Power, *108*.

Childs, D. W. and Vance, J. M., 1997, "Annular Gas Seals and Rotordynamics of Compressors and Turbines," *Proceedings of the Twenty-Sixth Turbomachinery Symposium*, Turbomachinery Laboratory, Texas A&M University, College Station, Texas, pp. 201-220.

Coleman, G. M., 1958, "Methods for the Measurement of Mechanical Impedance," Colloquial on Mechanical Impedance Methods of Mechanical Vibration, American Society of Mechanical Engineers.

DeCamillo, S. M., 2000, Private Communication—Journal and Thrust Bearing Temperature Data.

Edney, S. L., 1995, "Pad Temperature in High Speed, Lightly Loaded Tilting Pad Journal Bearings," *Proceedings of the Twenty-Fourth Turbomachinery Symposium*, Turbomachinery Laboratory, Texas A&M University, College Station, Texas, pp. 73-84.

Edney, S. L. and Mellinger, F. P., 1997, "Advances in Tilting Pad Journal Bearing Design," Dresser-Rand Technology Conference, Corning, New York.

Ewins, D. J., 1984, *Modal Testing: Theory and Practice*, Letchworth, Hertfordshire, England: Research Studies Press.

Greathead, S. and Bostow, P., 1976, "Investigations into Load Dependent Vibrations of the High Pressure Rotor on Large Turbo-Generators," Proceedings of the Institution of Mechanical Engineers Conference on Vibrations in Rotating Machinery, Cambridge, England.

Haq, I. U., Kumar, C. V., and Al-Zaid, R. M., 1998, "Identification of the Intermittent Synchronous Instability in a High Performance Steam Turbine Rotor Due to Deteriorated Labyrinth Seals," American Society of Mechanical Engineers, 98-GT-305.

Iwatsubo, T., 1980, "Evaluation of Instability Forces of Labyrinth Seals in Turbines or Compressors," Rotordynamic Instability Problems in High Performance Turbomachinery, NASA CP No. 2133, Proceedings of a Workshop Held at Texas A&M University.

Kurohashi, T., Inoue, Y., Abe, T., and Fujikawa, T., 1980, "Spring and Damping Coefficients of the Labyrinth Seals," Paper No. C283/80, Proceedings of the Second Institution of Mechanical Engineers Conference on Vibrations in Rotating Machinery, Cambridge, England.

Leie, B. and Thomas, H., 1980, "Self-Excited Rotor Whirl Due to Tip-Seal Leakage Forces," Rotordynamic Instability Problems in High Performance Turbomachinery, NASA CP No. 2133, Proceedings of a Workshop held at Texas A&M University.

Mikula, A. and Gregory, R., 1981, "A Comparison of Thrust Bearing Lubricant Supply Methods," ASME Journal of Lubrication Technology, *105*.

Mancuso, J. R., Gibbons, C. B., and Munyon, R. E., 1989, "The Application of Flexible Couplings for Turbomachinery," *Proceedings of the Eighteenth Turbomachinery Symposium*, Turbomachinery Laboratory, Texas A&M University, College Station, Texas, pp. 141-168.

Nicholas, J. C., 1989, "Operating Turbomachinery On or Near the Second Critical Speed in Accordance with API Specifications," *Proceedings of the Eighteenth Turbomachinery Symposium*, Turbomachinery Laboratory, Texas A&M University, College Station, Texas, pp. 47-54.

Nicholas, J. C. and Barrett, L. E., 1986, "The Effect of Bearing Support Flexibility on Critical Speed Prediction," ASLE Transactions, *29*, (3).

Nicholas, J. C., Edney S. L., Kocur, J. A., and Hustak, J. F., 1997, "Subtracting Residual Unbalance for Improved Test Stand Vibration Correlation," *Proceedings of the Twenty-Sixth Turbomachinery Symposium*, Turbomachinery Laboratory, Texas A&M University, College Station, Texas, pp. 7-18.

Nicholas, J. C., Whalen, J. K., and Franklin, S. D., 1986, "Improving Critical Speed Calculations Using Flexible Bearing Support FRF Compliance Data," *Proceedings of the Fifteenth Turbomachinery Symposium*, Turbomachinery Laboratory, Texas A&M University, College Station, Texas, pp. 69-78.

Pollman, E. and Termuehlen, H., 1975, "Turbine Rotor Vibrations Excited by Steam Forces," ASME Paper 75-WA/Pwr-11.

Scharrer, J. K. and Pelletti, J. M., 1995, "Leakage and Rotordynamic Effects of Compressible Annular Seals," *Proceedings of the Twenty-Fourth Turbomachinery Symposium*, Turbomachinery Laboratory, Texas A&M University, College Station, Texas, pp.175-190.

Singh, M. P., Vargo, J. J., Schiffer, D. M., and Dello, J. D., 1988, "SAFE Diagram—A Design and Reliability Tool for Turbine Blading," *Proceedings of the Seventeenth Turbomachinery Symposium*, Turbomachinery Laboratory, Texas A&M University, College Station, Texas, pp. 93-102.

Sohre, J. S., 1975, "Steam Turbine Blade Failures, Causes and Correction," *Proceedings of the Fourth Turbomachinery Symposium*, Turbomachinery Laboratory, Texas A&M University, College Station, Texas, pp. 9-30.

Thomas, H., 1958, "Instabile Eigenschwingungen von Turbinenläufern, Angefacht durch die Spaltströmungen, Stopfbüchsen und Beschaufelungen," Bull de L'AIM, *71*.

Urlichs, K., 1976, "Die Spaltströmung bei Thermischen Turbo-Machinen als Ursache für die Entstehung Schwingungsanfacher Querkräfte," Ingenieur-Archiv, *45*.

Williams, B. P. and Flack, R. D., 1993, "The Calculation of Rotordynamic Coefficients for Labyrinth Seals—A Manual for the Computer Program LABY3," ROMAC Report No. 344, University of Virginia.